51. Magnetic Information-Storage Materials

The purpose of this chapter to review the current status of magnetic materials used in data storage. The emphasis is on magnetic materials used in disk drives and in the emerging technology of the magnetic random-access memory (MRAM). A wide range of magnetic materials is essential for the advance of magnetic recording both for magnetic recording heads and media, including high-magnetization soft-magnetic materials for write heads, new antiferromagnetic alloys with high blocking temperatures and low susceptibility to corrosion for pinning films in giant-magnetoresistive (GMR) sensors and new ferromagnetic alloys with large values of giant magnetoresistance. For magnetic recording media, the advances are in high-magnetization metal alloys with large values of the switching coercivity. A significant limitation to magnetic recording is found to be the superparamagnetic effect and new advances in multilayer ferromagnetic films to reduce the impact of the effect, but also to allow high-density recording have been developed.

Perpendicular recording as compared to longitudinal recording is reviewed and it is shown that this technology will be the dominant recording technology in the future. The MRAM device uses some of the same materials as used in the GMR sensor, but the key technology is the magnetic tunneling junction in which soft-magnetic films are coupled by a thin insulating film and conduction is by quantum-mechanical tunneling. The status of the MRAM technology and some of the key problems are reviewed.

The purpose of this chapter is to summarize the status of magnetic materials used in high-capacity disk drives and magnetic-semiconductor memory devices. The technology of disk drives is selected since these devices have experienced the largest increase in data capacity over time and this has made disk drives the preeminent storage system for digital data. To illustrate this point, consider Fig. 51.1, which is a plot of the areal density (number of data tracks per inch times the number of bits per inch recorded on a track) for disk drives over time [51.1]. The increase in areal density is more than 100% per year up to about 2002, when it reduced to about 20–30%. At the time of writing the areal density being shipped in disk drives is close to 130 Gb/in^2. The total data capacity of a disk is approximately the areal density times the recording area, which depends on the size of the disk [2.5 and 3.5 inches (64 and 90 mm)] diameter being the most common. Many technologies have contributed to this rapid increase in areal density, including advances in the technology of *flying* heads with reduced spacing to the disk surface, data codes and error detection and correction, advanced servo control systems for accurate control of magnetic recording heads on data tracks, and improvements in the mechanical structures comprising a disk drive, including advances in motors used to drive the disks. However, this paper discusses only the fundamental technology associated with digital magnetic recording, including the devices used to record and read back the recorded data and the media on which the data is recorded. The discussion is also restricted to the materials and not to any of the mechanical structures associated with the recording heads or disks. The discussion covers conventional longitudinal magnetic recording as used in present (and past) disk drives

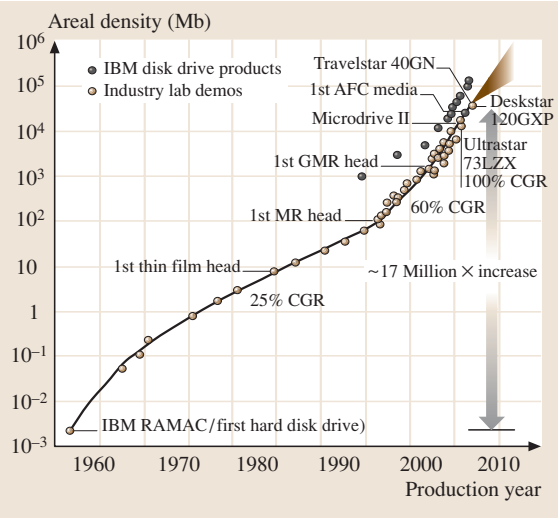

Fig. 51.1 IBM areal density perspective. (After [51.1])

and the emerging technology of perpendicular magnetic recording, in which the remanent magnetization is perpendicular to the disk surface, and which reduces the impact of the superparamagnetic limit (to be discussed). We will not discuss some variants of longitudinal magnetic recording, e.g., thermally assisted recording and patterned media.

Recently there has been a significant new emerging technology for fast memory devices – magnetic random-access memory (MRAM). The MRAM device is a possible replacement for the familiar semiconductor memories used in modern computers – dynamic and static random-access memory (DRAM and SRAM). The MRAM technology combines a magnetic storage technology together with metal-oxide semiconductor (MOS) devices to result in fast and high-density data memory devices. The technology on which the magnetic part of MRAM is based is an extension of the technology used in magnetic recording devices – the magnetic tunneling junction (MTJ). The MRAM technology will also be discussed in this paper. Parts of this chapter have been previously published in the Journal of Materials Science: Materials in Electronics [51.2].

51.1 Magnetic Recording Technology

The technology of magnetic recording was one hundred years old in 1999 [51.3]. The fundamental concept of magnetic recording is to use a magnetic structure (the *write head*) driven by current which represents the data to be recorded to generate a magnetic field which can change the state of the magnetization in a closely spaced magnetic recording medium, which in the earliest realization was magnetic wire, and today is either the familiar magnetic tape or a magnetic layer on a rigid disk substrate. The data are recovered by the generation of an output voltage in the *read head* by sensing the magnetization in the recording medium, e.g., by Faraday's law ($V = N\frac{d\Phi}{dt}$), where N is the number of turns on the read head and Φ is the magnetic flux coupled to the read head from the media. The magnetic recording system to be discussed here is that used to store digital data, in which case the current supplied to the write head is in the form of pulses encoded to represent the digital data (1s or 0s) [51.4, 5]. In the case of disk drives the

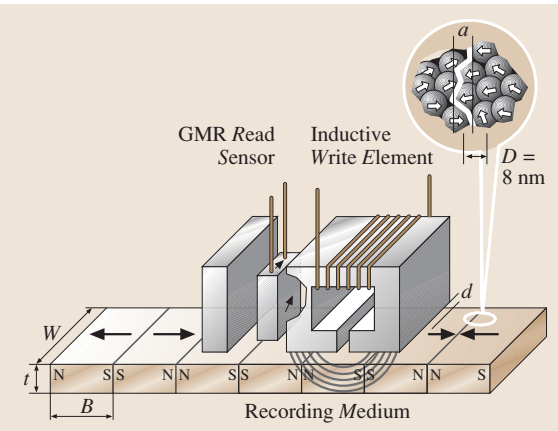

Fig. 51.2 Schematic illustration of a longitudinal magnetic recording system showing a giant magnetoresistive (GMR) read sensor, write element and the recording medium. The parameters are: t the recording medium thickness (δ is also used), W the width of the recorded track, B the length of the recorded magnetization or bit size and d the magnetic spacing (includes overcoats on the disk surface and undercoats on the slider surface). Shown in the *inset* is the transition region between the two directions of the magnetization; D is the media grain size and a is the transition parameter that characterizes the length of the transition region (length $l = \pi a$). (After [51.1])

write and read heads are separate thin-film structures deposited on the back of a mechanical slider, which uses a hydrodynamic air bearing to *fly* over the surface of the disk [51.5]. Figure 51.2 is a schematic of a modern digital magnetic recording system. The recording (*write*) and read elements are shown together with the magnetic recording surface which in modern disk drive technology is a thin metallic film of a cobalt alloy (to be discussed). The digital data are recorded in the magnetic film as *transitions* between the two possible states of the magnetization (pointing to the *left* or *right*) and with the width approximately equal to the width of the write head and the width of a data track. The transition region between the oppositely directed directions of the magnetization is similar to that between magnetic domains and has a length l. We will discuss the different parts of the recording system starting with the write head and including the read head which in Fig. 51.2 is a giant-magnetoresistive sensor. First, we will discuss some aspects of thin magnetic films that are relevant to magnetic recording components. All magnetic recording components used in disk drives today are fabricated from thin films to allow mass production and for technology reasons, as we will discuss.

51.1.1 Magnetic Thin Films

Induced Uniaxial Anisotropy

In most applications of soft-magnetic films a uniaxial anisotropy in the plane of the film is required. One way of introducing this uniaxial anisotropy is to induce it by applying a magnetic field in the plane of the film and the effect is referred to as magnetic annealing. The anisotropy can be induced during deposition of the film or induced by a subsequent annealing step, using temperature and a magnetic field to modify the anisotropy. The mechanism of the induced anisotropy is that of directional order, in which atomic pairs in an alloy tend to align with the local magnetization. In nickel–iron films the atomic pairs are the iron atoms and the induced uniaxial anisotropy energy density is typically $K_u \cong 1\text{–}3\,\mathrm{kerg/cm^3}(0.1\text{–}0.3\,\mathrm{kJ/m^3})$, where the uniaxial energy density is

$$E_k = K_u \sin^2\theta\,, \tag{51.1}$$

where θ is the angle of the magnetization with respect to the direction of the induced anisotropy. To induce the anisotropy it is necessary to saturate the magnetization of the film with a small magnetic field, typically 50–100 Oe (4000–8000 A/m), since it is the magnetization not the magnetic field that is responsible for the magnetic annealing. If the anisotropy energy density is positive the energy is minimum is along the direction of the anisotropy, which is referred to as an *easy* axis.

A second method of introducing uniaxial anisotropy in thin films is by stress. If the magnetostriction constant is isotropic with value λ_s for a polycrystalline material then the magnetoelastic energy density is given by

$$E_{me} = \frac{3}{2}\lambda_s\sigma\sin^2\theta\,. \tag{51.2}$$

The angle θ is the angle of the magnetization in the film plane with respect to the direction of the stress (σ). If a sample is unmagnetized it will strain by λ_s as the sample is magnetized to saturation. A typical value of λ_s is $\approx 10^{-6}$. If the magnetostriction constant and the stress are both positive the direction for the minimum energy and hence the easy axis is for $\theta = 90°$. The magnetization, permeability, crystalline anisotropy constant and magnetostriction constant of nickel–iron alloys $Ni_xFe_{(1-x)}$ are shown in Fig. 51.3 [51.6]. The maximum permeability is for the Permalloy composition $Ni_{80}Fe_{20}$. Increasing the atomic percentage of iron over that of Permalloy results in increased magnetization since the magnetic moment for iron is 2.2 μ_B (Bohr magnetons) per atom in the metal, while the value for nickel is 0.6 μ_B per atom in the metal.

Hysteresis in Soft-Magnetic Films

If we impose an external magnetic field H_e along the direction of the induced anisotropy (easy axis) of the thin film ($\theta = 0°$) the total energy density is given by

$$E_k = K_{eff}\sin^2\theta - MH_e\cos\theta\,.$$

K_{eff} is the sum of the uniaxial crystalline anisotropy (K_u) and the stress anisotropy ($3/2\lambda_s\sigma$). The second term is the magnetostatic energy. The equilibrium angle for the magnetization is given by minimizing the total energy,

$$\frac{dE}{d\theta} = 2K_{eff}\sin\theta\cos\theta + MH_e\sin\theta = 0\,.$$

The solution $\sin\theta = 0$ implies that the magnetization lies at either $\theta = 0$ or 180°. However, the energy must be a minimum for stability and the second derivative changes sign at a boundary between stability and instability

$$\frac{d^2E}{d\theta^2} = 2K_{eff}(\cos^2\theta - \sin^2\theta) + MH_{e,crit}\cos\theta = 0\,.$$

The magnetic field which just satisfies this condition is

$$H_{e,crit} = -H_c = -\frac{2K_{eff}}{M}\,. \tag{51.3}$$

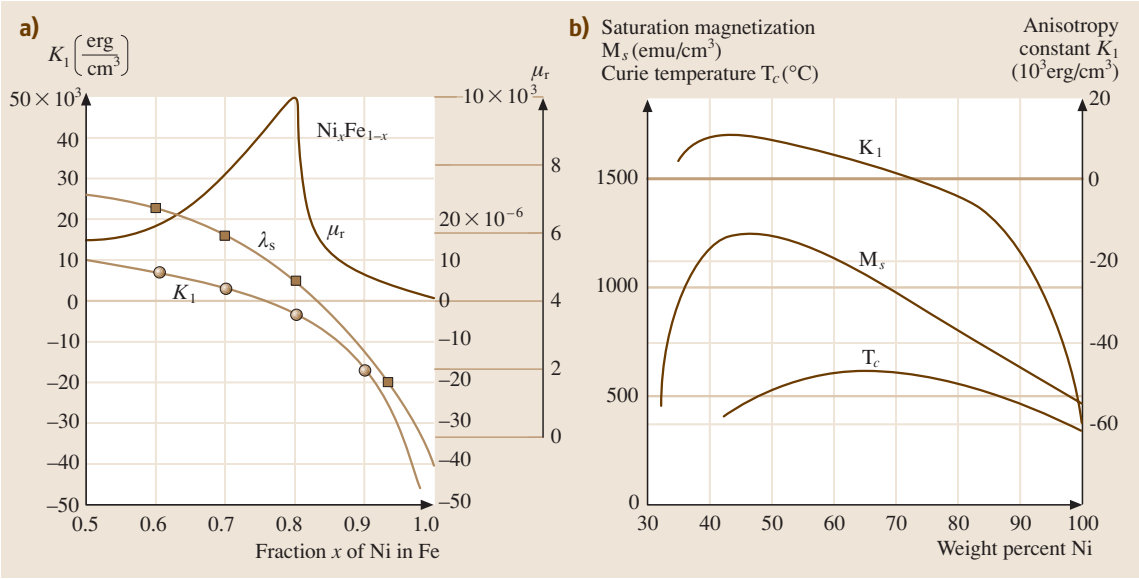

Fig. 51.3 **(a)** Magnetic properties of Ni_xFe_{1-x} alloys, including initial permeability, crystalline anisotropy and magnetostriction. **(b)** Magnetization, Curie temperature and crystalline anisotropy of Ni_xFe_{1-x} alloys. (After [51.6])

The critical magnetic field is the coercive field (H_c). A curve of the magnetization versus applied magnetic field for this case is shown in Fig. 51.4 (curve labeled "easy"), which was measured on a thin film of FeCoNi (to be discussed) [51.7]. The magnetization curve exhibits hysteresis and in the FeCoNi alloy the coercive field is small and the material is magnetically *soft*. Hysteresis is responsible for the use of magnetic materials as digital memory devices since the *up* or positive state of the magnetization could represent a binary 1 and the *down* or negative state could represent a binary 0 and these states can be stable even in zero applied field ($H_e = 0$). The above analysis also applies to magnetically hard films, for which the coercive field is large. We will discuss magnetic recording media and here the coercive field is measured in units of kOe.

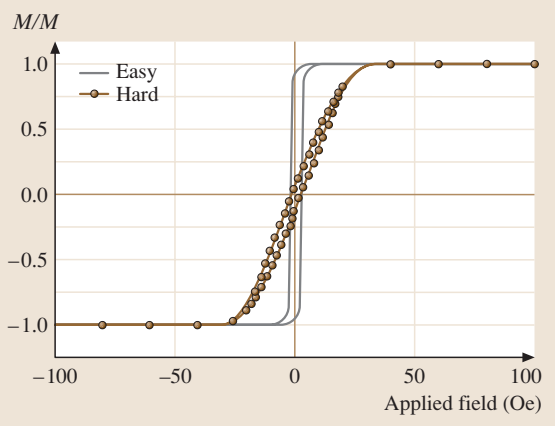

Fig. 51.4 Easy and hard magnetization curves of an electroplated FeCoNi alloy film. (After [51.7])

With the magnetic field applied perpendicular to the easy axis, along the hard axis, the energy density is given by

$$E_k = K_{\text{eff}} \sin^2\theta - MH_e \sin\theta \,.$$

The derivative of the total energy is given by

$$\frac{dE}{d\theta} = 2K_{\text{eff}} \sin\theta\cos\theta - MH_h \cos\theta = 0$$

resulting in the two solutions

1. $\cos\theta = 0$, or $\theta = 90°$ or $270°$;
2. $\sin\theta = \frac{H_h}{2K_{us}/M}$.

The solution to this case is also shown in Fig. 51.4 (curve labeled "hard") and is seen not to exhibit hysteresis. This is the *hard-axis* magnetization curve and the magnetic field where the magnetization saturates is known as the anisotropy field H_k. The hard-axis magnetization curve is used extensively for magnetic recording heads.

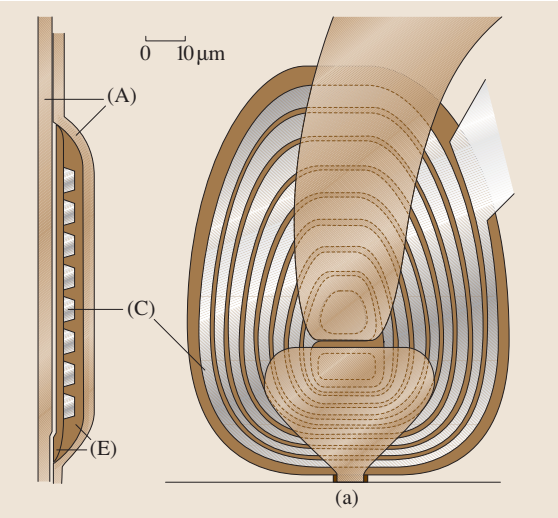

Fig. 51.5 Thin film head with eight turns showing the poles and yoke structure. A is Permalloy, C is copper and E is baked photoresist. (After [51.13])

51.1.2 The Write Head

The write head is formed from thin films of soft ferromagnetic alloys patterned in the form of a magnetic yoke. A schematic of an eight-turn thin-film head is shown as Fig. 51.5 [51.13]. Heads in present disk drives typically have fewer than five turns to reduce inductance. The cross-hatched regions are the soft ferromagnetic material and the leads which carry the write current are shown on the right-hand side of the top view. Note that the widths of the copper alloy turns are increased near the back region of the head to reduce resistance. The heads are fabricated using electroplating and the substrate (not shown) is a hard ceramic that can be machined to form the slider [51.5]. Electrical current in the form of pulses is coupled to the yoke to generate a magnetic field at the gap. The coil is insulated from the metallic magnetic yoke by layers of baked polymer photoresist. The alloy that has been used most frequently in the past for the magnetic films in the write head is $Ni_{80}Fe_{20}$ – Permalloy, which can be deposited in thin films using electroplating. Electroplating is discussed in *Comstock* [51.4] and in more detail by *Andricacos* and *Romankiw* [51.14]. The maximum coercivity ($H_{c,max}$) of the recording medium that can be recorded by the write head is given by (51.4) (in cgs units) [51.4]

$$H_{c,max} = 0.20 \times 4\pi M_s \tan^{-1}\left(\frac{g/2}{d+\delta}\right) , \qquad (51.4)$$

where $4\pi M_s$ (Gauss) is the saturation flux density of the material used in the recording or write head, g is the gap length of the write head, d is the *magnetic spacing*, which is the spacing of the head to the recording magnetic film (including any overcoat films on the recording heads and recording medium) and δ is the thickness of the recording film (shown as t in Fig. 51.2). To increase the linear density (transitions along a recorded track), it is necessary to increase the coercive field of the recording media. This is the case since the length of a transition between the two states of the magnetization is given by (51.5) (in cgs units) [51.15] and [51.4].

$$l = \pi a = \pi\left(\frac{d\,(1-S^*)}{\pi Q}\right) + \left[\left(\frac{d\,(1-S^*)}{\pi Q}\right)^2 + \left(\frac{2M_r\delta}{H_c}\right)\left(\frac{2d}{Qr}\right)\right]^{1/2} , \qquad (51.5)$$

where $S^* = 1 - \frac{M_r/H_c}{dM/dH(H=-H_c)}$ quantifies the slope of the hysteresis curve of the recording medium at the coercive field and $Q = \frac{dH_x/dx}{H_c/d}$; Q is the normalized slope of the horizontal component of the write-head magnetic field at the value $H = H_c$. A typical value of Q is 0.7.

Table 51.1 Properties of materials used in magnetic recording heads

Material	B_s(kG) ($T\times10^{-1}$)	μ_r	ρ ($\mu\Omega$cm)	H_c (Oe) (A/m)	References
$Ni_{80}Fe_{20}$ (Permalloy)	10	1500–3000	20	0.1–0.5 (7.95–39.78)	[51.6]
Sendust (FeSiAl)	10	8000	85	0.25 (19.9)	[51.4]
$Ni_{45}Fe_{55}$	16	1700	48	0.3 (23.87)	[51.8]
$Co_{48}N_{22}Fe_{30}$ electroplated with pulsed plating	21.5	1000	–	≈ 1 (79.6)	[51.9]
$Co_{56}Ni_{13}Fe_{31}$(C) electroplated with carbon impurity	19	–	≈ 70	≈ 2 (159.2)	[51.10]
FeAl(2%Al)N (N/Fe 6.6%) sputtered	20	2450	38	3.8 (302.4)	[51.11]
FeTiN sputtered	18–21	–	–	≈ 5 (397.9)	[51.12]

M_r (emu/cm^3) is the remanent magnetization of the recording medium with thickness δ.

From (51.4) and (51.5) it is seen that for reduced transition length (and hence higher linear density) it is necessary to increase the coercive field (H_c) of the recording medium but to do so requires a concomitant increase in the magnetization of the write head (51.4). Materials with magnetization larger than Permalloy [$4\pi M_s = 10\,\text{kG}$ ($M_s = 1\,\text{T}$)] and which are magnetically soft (large permeability) are listed in Table 51.1. The most common material used in present disk drives is electroplated $Ni_{45}Fe_{50}$, with a saturation magnetization of $4\pi M_s = 16\,\text{kG}$ ($M_s = 1.6\,\text{T}$) [51.8]. Ternary alloys of Ni, Fe and Co also can be electroplated with saturation magnetization of $4\pi M_s \geq 20\,\text{kG}$ ($M_s = 2\,\text{T}$). The composition region that results in the largest value of saturation magnetization but also large permeability is: $Co_{48-56}Fe_{30-31}Ni_{22-13}$ (Table 51.1). A useful guide to the selection of the composition of the ternary FeCoNi alloys is the composition diagram shown as Fig. 51.6 [51.6]. The data for Fig. 51.6 were accumulated in bulk materials. In a study of electroplating FeCoNi alloys for write heads [51.7] care was taken to avoid any impurities in the plating bath and the results showed the possibility of achieving $4\pi M_s$ values in the range of 21–21.5 kG and $H_c < 2\,\text{Oe}$ in the same region of the composition diagram (approximately $Fe_{35}Co_{45}Ni_{20}$). However, experiments in a larger cell in conditions closer to those in a manufacturing plating system and with higher Fe content and an organic additive ascorbic acid used to reduce the formation of Fe^{3+} showed even larger values of $4\pi M_s$ ($> 2.2\,\text{kG}$) but with increased coercivity ($> 8\,\text{Oe}$) [51.16]. The composition of ferromagnetic alloys can be selected to result in zero values for the magnetostriction constant and the Permalloy composition of nickel–iron alloys ($Ni_{80}Fe_{20}$) has a zero magnetostriction constant (Fig. 51.3). The magnetostriction constant is frequently chosen to be small and negative so that the magnetoelastic energy defines an easy axis at right angles to the direction of the stress [$\theta = 90°$ in (51.2)]. In the case of thin-film write heads the stress is along the axis of the poles (upward in the

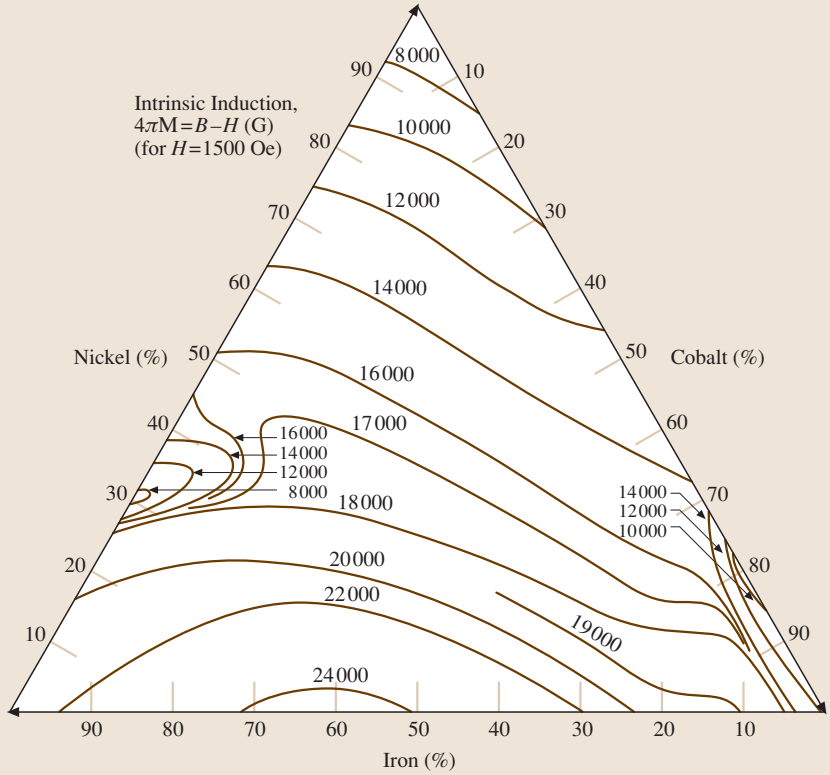

Fig. 51.6 FeCoNi saturation magnetization contours. (After [51.6])

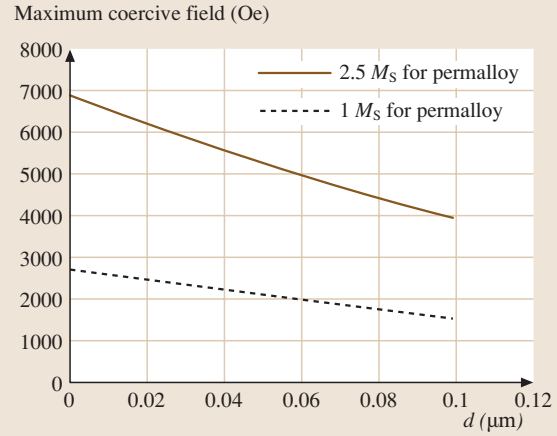

Fig. 51.7 Maximum coercivity of recording media versus magnetic spacing (d) for write heads fabricated from Permalloy and from a magnetic material with saturation magnetization 2.5× Permalloy

patterned yoke in Fig. 51.5) and with negative magnetostriction constant the easy axis is across the pole width, which means that the direction of flux flow is along the hard axis with the desired linear relation between the magnetization and the magnetic field (Fig. 51.4). In the case of the ternary alloys of FeCoNi an alloy composition that results in zero magnetostriction is $Fe_{13}Co_{31}Ni_{56}$, in which the nickel content is too high to be a useful write-head material [51.7].

Alloys of FeAl (2% Al) [51.11] and FeTi (≈ 2% Ti) [51.12] sputtered using a mixed N and Ar working gas offer desirable magnetic properties, as shown in Table 51.1, but have not replaced the electroplated alloys because of increased costs of sputtering. A material of interest for even higher values of saturation magnetization is the α'' phase of $Fe_{16}N_2$, which has a potential of a saturation magnetization of 29 kG; however, this phase is metastable [51.18]. The actual values of saturation magnetization with this phase in thin-film form was 20 kG and required annealing at 200 °C [51.18].

To record on recording media with increased coercivity is not the only issue with the magnetic materials used in write heads. It is also important that the write heads have high efficiency. Efficiency (η) in this case is defined as the ratio

$$\eta = \frac{H_g g}{N_w I} , \qquad (51.6)$$

where H_g is the value of the magnetic field in the gap of the write head and I is the amplitude of the write current pulse. High efficiency is important to allow write-current amplitudes that are easily supplied from integrated circuits. For high efficiency it is necessary that a large percentage of the magnetomotive force ($N_w I$) results in a magnetic field across the gap. However, the permeability of the yoke influences the efficiency

$$\eta = \frac{g/A_g}{g/A_g + l_c/\mu_r A_c} , \qquad (51.7)$$

where A_g and A_c are the area of the gap and core, respectively; l_c is the length of the core and μ_r is the relative permeability of the core or yoke material. As shown in Fig. 51.3, the relative permeability (μ_r) of nickel–iron alloys drops for compositions different from the Permalloy composition. This decrease in the permeability of nickel–iron alloys with composition different from that for Permalloy is the direct result of the increase in crystalline anisotropy and magnetostriction, as shown in Fig. 51.3. The lower permeability of the FeCoNi alloys can be obviated in a design of the write head in which the high-magnetization films are used only in the gap region in a design referred to as a *stitched* head.

The values of coercivity of the recording medium (H_c) that can be recorded with recording heads with the saturation magnetization of Permalloy [$4\pi M_s$ = 10 kG (M_s = 1 T)] and materials with saturation magnetization 2.5 times that for Permalloy [$4\pi M_s$ = 25 kG (M_s = 2.5 T)] are shown versus the magnetic spacing (d) in Fig. 51.7. The magnetic spacing for recent technology demonstrations has reached a value of 15 nm (carbon overcoat for head – 3 nm, pole tip recession tolerance – 3 nm, flying height – 5 nm, and media

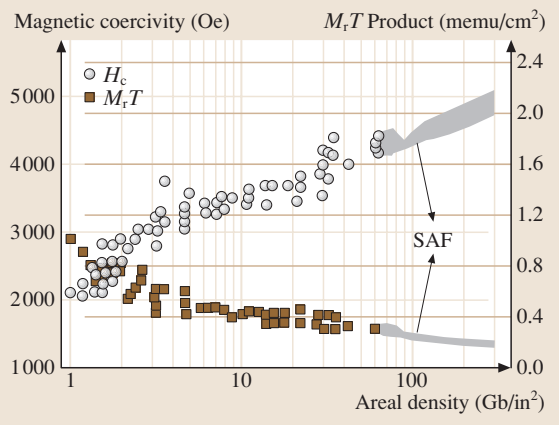

Fig. 51.8 Trend in coercive field (H_c) and media flux (M_rT) versus areal density in Gb/in^2 for disk drives. (After [51.17])

carbon overcoat – 4 nm). The trend in coercivity (H_c) and flux ($M_r\delta$ or M_rT) versus areal density in commercial disk media is shown as Fig. 51.8 [51.17]. We will discuss synthetic antiferromagnetic media (SAF) media later.

With the increased linear density associated with increased areal density in disk drives and with increases in the rotation speed of the disks, the rate at which data are recorded (and read back) has increased over time. This increase in data rate leads to a requirement that the magnetic fields in the gap of a write head switch in ever decreasing times. The switching time of thin magnetic films as used in write heads is limited by three factors: first, the fundamental switching time resulting from the fact that magnetic moments are always associated with angular momentum that cannot be changed instantaneously; second, the eddy currents associated with the changing magnetic fields both decrease the magnetic fields and slow down the switching speed, and third the inductance of the coil [51.21]. Data rates depend on the form factor of the disks and with high-end 3.5-in drives the data rates are larger than 50 Mb/s, while with 2.5-in drives the data rates are roughly one-half as large.

51.1.3 Spin Valve Read Head

The technology that has evolved for sensing or reading the flux emanating from transitions in thin-film disk media is the spin valve. This technology is based on the giant-magnetoresistive (GMR) effect discovered in France and published in 1988 [51.19]. GMR results when thin ferromagnetic films are coupled by an even thinner spacer film of a nonmagnetic transition metal. A curve of resistance normalized to that with no magnetic field applied versus magnetic field for arrays of ferromagnetic films of Fe with thickness of 30 Å (3 nm) coupled by Cr with thickness varying from 9–18 Å (0.9–1.8 nm) is shown in Fig. 51.9 [51.19]. The number subscripted to the parenthesis characterizing the magnetic and transition-metal films is the number of such films, which are referred to as *superlattices*. With no applied magnetic field, the two films were antiferromagnetically coupled; that is, the magnetizations in the two films are equal in magnitude and oppositely directed. The application of a large in-plane magnetic

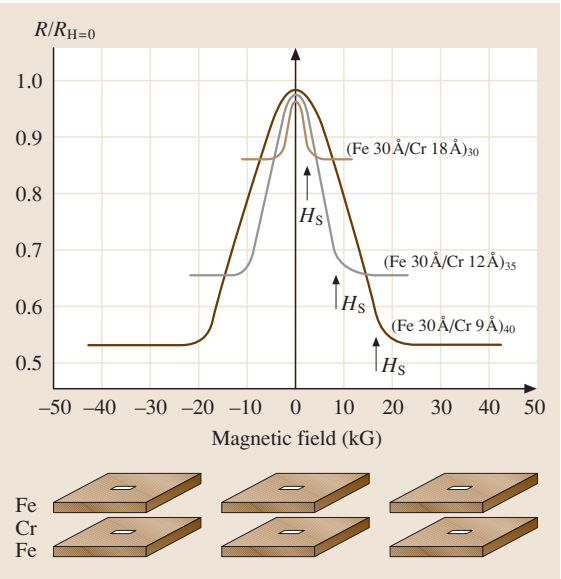

Fig. 51.9 The magnetoresistance of three $(Fe/Cr)_n$ superlattices at 4.2 K. The thickness of the layers in angstroms is shown. (After [51.19])

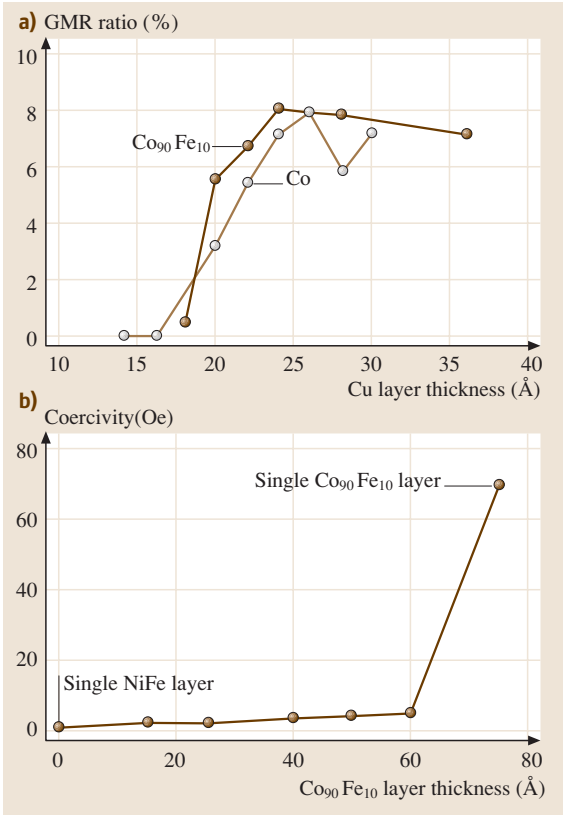

Fig. 51.10 **(a)** Comparison of GMR ratio ($\Delta\rho/\rho$) as a function of copper layer thickness in $Co_{90}Fe_{10}$ and Co films (see text). **(b)** Coercivity as a function of $Co_{90}Fe_{10}$ layer thickness in Ta (50 Å)/[$Ni_{80}Fe_{20}$/$Co_{90}Fe_{10}$] (75-Å) films. (After [51.20])

field rotated the magnetization of the coupled films to a parallel configuration, reducing the resistance (to be discussed). The current used to measure the magnetoresistance – the change in resistance with applied magnetic field – is applied in the plane of the films. This orientation of current is referred to as current-in-plane (CIP). Later we will discuss an alternative orientation of the current – current-perpendicular-to-plane (CPP). The initial discovery of GMR was done with a temperature of 4.2 K and the magnetic fields applied were measured in kOe ($10^6/4\pi$ A/m). The large change in resistance with magnetic field was in contrast to that observed in the anisotropic magnetoresistance (AMR) effect, which is the change in resistance observed when the magnetization in a *single* ferromagnetic film is rotated from an easy toward a hard axis. This latter technology – for which the resistance change with Permalloy was of the order of 2–3% – was being used in read heads during the time of research on the GMR effect. By the early 1990s it was found possible to observe GMR in other film materials with increased spacer film thickness at 300 K and with magnetic fields of tens of Oersteds. For example, the GMR ratio for two coupled films of an alloy of cobalt and iron ($Co_{90}Fe_{10}$ for which the magnetostriction constant is zero) with a variable thickness of the spacing layer of copper is shown in Fig. 51.10a [51.20]. It is seen that the GMR ratio is considerably reduced from that for the Fe/Cr superlattices at 4.2 K (Fig. 51.8) but the ratio is larger than that for the AMR effect. The discovery of the GMR effect led to the invention of the *spin valve read head*, in which one of two ferromagnetic films coupled by a thin transition-metal film is maintained constant in direction (the *pinned* film) and the orientation of the other film (the *free* film) is allowed to rotate (in the plane of the magnetic film), resulting in a decrease in resistance [51.22]. We will discuss the technology of pinning later. By free, it is meant that the magnetization in the film is easily rotated, e.g., by the magnetic field arising from transitions in the recording medium. It is surprising that cobalt is found to be useful in this application since cobalt is magnetically hard (pure cobalt metal has a high coercivity and is used in recording surfaces) and one of the requirements for the GMR effect is that the free film have high permeability and high efficiency (51.6). The reason for this result is shown in Fig. 51.10b, where the coercivity of a free film consisting of two films: $Ni_{80}Fe_{20}$ [60 Å (6 nm)] and $Co_{90}Fe_{10}$ is plotted versus the thickness of the $Co_{90}Fe_{10}$ film [51.20]. Even though the cobalt alloy would have a large coercivity in the bulk, the coercivity for thin films, together with the underlying $Ni_{80}Fe_{20}$ film, is low for thicknesses less than about 60 Å. The advantage of the cobalt–iron film is the increased GMR ratio over $Ni_{80}Fe_{10}$. In order to increase the GMR ratio even more it has been found advantageous to deposit an interfacial nanolayer of cobalt metal on one or both sides of the free film [51.23]. We will learn in a discussion of the origin of GMR that cobalt has the potential for large GMR ratios.

A schematic of the spin valve read head is shown as Fig. 51.11 [51.22]. The magnetization of the free film is shown rotated to an angle θ_1 and the pinned layer is shown with a fixed angle of θ_2. The pinning effect is due to the coupling of the pinned film to an underlying antiferromagnetic film as we will discuss. The nonmagnetic spacing layer separates the two ferromagnetic films. The maximum output voltage for the spin valve with no external resistance (and no reduction in the flux due to shielding (to be discussed) is

$$\Delta V = \eta J W_r \Delta\rho \,(1 - \sin\Delta\theta_1)\,/2\,, \qquad (51.8)$$

where η is the efficiency of the read head, which accounts for the fact that the angle θ_1 is not uniform over the height of the free film, J is the density of the current flowing through the films, W_r is the width of the read head (always less than the width of the written track) and $\Delta\rho$ is the change in resistivity of the stack of films with a change of θ_1 from $-90°$ to $+90°$, again with θ_2 fixed. The factor of 2 in the denominator is the result of the actual rotation of θ_1 being limited to 0° to 90°. The device senses magnetic field in the plane of the free film resulting from transitions in the recorded media ($H_{y,\text{disk}}$)

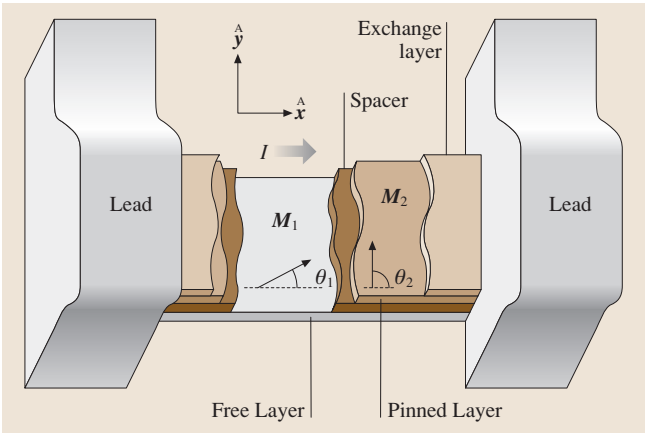

Fig. 51.11 Schematic of spin valve read element. The magnetization of the free layer is shown at an angle θ_1 to the easy axis (and direction of the current) and the magnetization of the pinned layer is fixed at 90° to this axis. (After [51.22])

through the rotation of the magnetization in the free film

$$\sin\theta_1 = \frac{H_{y,\mathrm{disk}}}{H_\mathrm{k}}\,, \tag{51.9}$$

where H_k is the anisotropy field of the free film (see analysis of the hard-axis magnetization curve in Sect. 51.1.1). In the absence of any other magnetic fields, the magnetization will lie along the easy axis. The hard axis is perpendicular to the easy axis. The voltage is measured across the lead terminals using a sense current and the width of the track is just the spacing between the leads. A typical value of peak output voltage per unit of track width for presently used spin valves is 15 mV/μm. Spin valve read heads are shielded on each side of the stack of films to realize a narrow pulse width. The total width between the shields is G and the thickness of the stack of films comprising the spin valve is t. The read pulse is characterized by the amplitude but also by the width at one-half amplitude (PW_{50} in distance units) (discussed in [51.4])

$$PW_{50} \approx \sqrt{\frac{1}{2}\left(G^2+t^2\right)+4\,(d+a+\delta/2)^2}\,, \tag{51.10}$$

where G is the total spacing between the shields and δ is the thickness of the recording layer.

The peak voltage amplitude with the shields with no external resistance can be approximated by

$$V_\mathrm{GMR}(\mathrm{peak}) = \frac{\eta I\,\Delta R_\mathrm{max}\,M_\mathrm{r}^\mathrm{rec}\,\delta}{\pi t M_\mathrm{s}^\mathrm{GMR}}\left(\frac{(g+t)}{g}\right) \times 2\tan^{-1}\frac{g}{2(d+a)}\,,$$

$$I\,\Delta R_\mathrm{max} = JW_\mathrm{read}\,R_\mathrm{square}\,t_\mathrm{sv}\,\frac{\Delta R_\mathrm{max}}{R_0}\,, \tag{51.11}$$

where η is the read efficiency, defined as the fraction of the flux sensed by the head to the total flux, $M_\mathrm{r}^\mathrm{rec}$ is the magnetization of the recording layer, $M_\mathrm{s}^\mathrm{GMR}$ the saturation magnetization of the free layer, g is the half-gap between the shields, R_square is the resistance per square of the stack of films comprising the spin valve and t_sv is the thickness of the free layer (modified from [51.24]).

Pinning with an Antiferromagnetic Film

For a spin valve to function, the pinned ferromagnetic film must have its magnetization perpendicular to the recorded track, as shown in Fig. 51.11 (the vertical magnetic field from the transitions in the disk is in the y-direction). This orientation of the magnetization in the pinned film is achieved by coupling the ferromagnetic film to an antiferromagnetic film and the coupling results from the layer of spins in the antiferromagnetic film adjacent to the top layer of spins in the ferromagnetic film and is characterized by a coupling or exchange field of value H_ua. The geometry for the coupling is shown in Fig. 51.12a and the ferromagnetic film geometry with a magnetic field along the easy axis ($H_{||}$) and the hard axis ($H_\perp$) as Fig. 51.12b. The coupling results in shifting the easy axis hysteresis curve ($M_{||}/M_\mathrm{s}$ versus $H_{||}$) of the ferromagnetic film by an amount H_ua, as shown in Fig. 51.13 [51.4]. The magnetization of the pinned film is held constant at $-M_\mathrm{s}$ over the range of magnetic fields from large negative fields to $H_\mathrm{ua}+H_\mathrm{k}$. Note that the magnetization could be held at $+M_\mathrm{s}$ by reversing the direction of the lower layer of spins in the antiferromagnetic film. The coupling field depends on the temperature and vanishes at the *blocking* temperature. The direction of the coupling is established during an annealing step by heating the structure above the blocking temperature, where the film is paramagnetic, in the presence of a magnetic field and then cooling the film below the blocking temperature. The choice of

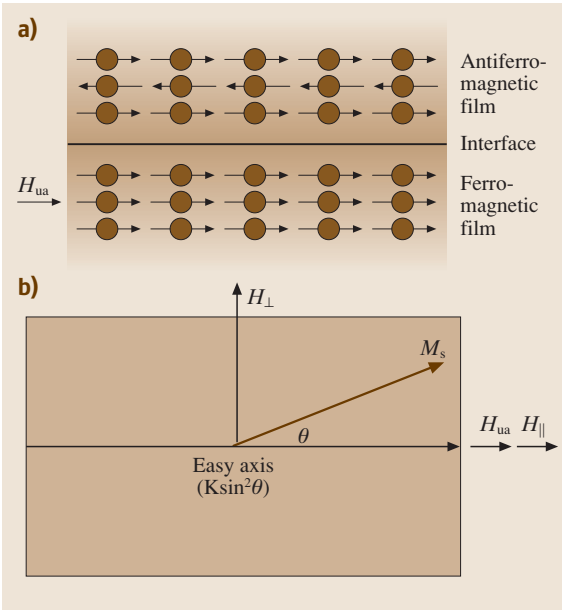

Fig. 51.12 **(a)** Schematic of the coupling of an antiferromagnetic to a ferromagnetic film. **(b)** Geometry of the ferromagnetic film showing the induced easy-axis field, H_ua, the external magnetic fields $H_{||}$ and $H_\perp$ and the magnetization of the film at an angle θ to the easy axis. (After [51.4])

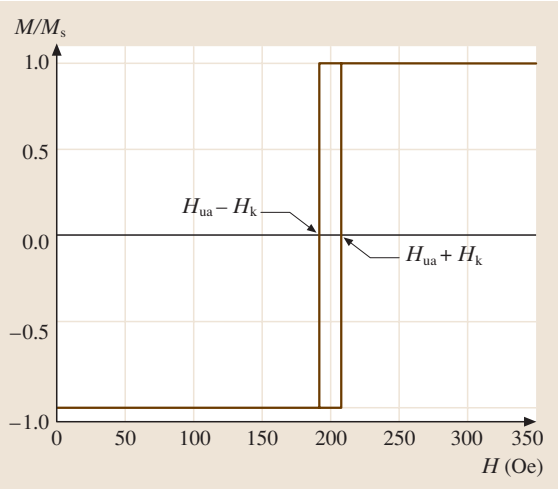

Fig. 51.13 Magnetization curve with the magnetic field along the easy axis ($M_{||}/M_s$ versus $H_{||}$) for coupled antiferromagnetic and ferromagnetic films. (After [51.4])

antiferromagnetic films to be used in this application is extensive as shown in Table 51.2 [51.25–28]. The parameters listed in Table 51.2 are the strength of the coupling field (H_{ua}), the blocking temperature and the susceptibility of the antiferromagnetic and ferromagnetic films to corrosion. Corrosion is of concern in recording heads because of the mechanical lapping process used to form the surface on the bottom of the slider on which the air-bearing contour is etched [51.5]. One antiferromagnetic film with particularly favorable corrosion susceptibility is NiO. This film is typically used in a bottom spin valve in which the antiferromagnetic film is closest to the substrate. The other antiferromagnetic films are typically formed on top of the stack of films. Another advantageous film is the alloy of $Pd_{30}Pt_{20}Mn_{50}$ [51.28]. This ternary alloy has a favorable coupling strength H_{ua} but also a high blocking temperature (300 °C) and favorable corrosion resistance. $Pd_{30}Pt_{20}Mn_{50}$ does require annealing the stack at 220–240 °C. The advantage of using an antiferromagnetic film for the pinning film instead of a permanent magnetic film is that the antiferromagnetic film does not itself respond to any external magnetic field since the film has a zero net magnetization.

Synthetic Antiferromagnets

The magnetic coupling between magnetic films closely spaced by certain nonmagnetic metal films oscillates between antiferromagnetic and ferromagnetic coupling. Using this fact, it is possible to design film structures that have a desired magnitude and sign of the magnetic coupling [51.29]. A schematic of a structure of films that exhibits this variable coupling is shown in Fig. 51.14a. Here the strong antiferromagnetic coupling of Co through Ru to soft $Ni_{80}Co_{20}$ is used to pin the magnetization in the adjacent $Ni_{80}Co_{20}$ film (F_I) to the direction opposite to the Co film and the thickness of the second layer of Ru can be adjusted to change the sign of the coupling between the two soft-magnetic films (F_I and F_{II}). Ruthenium is selected for the coupling film since it has a strong and oscillating coupling between Co, $Ni_{80}Fe_{20}$ and $Ni_{80}Co_{20}$. Ruthenium has the hexagonal close-packed (hcp) crystal structure with ($a = 0.271$ nm and $c = 0.428$ nm) while cobalt also has the hcp structure with ($a = 0.250$ nm and $c = 0.410$ nm) and therefore the two metals are expected to grow epitaxially. The experimental coupling constant (J_{12}) for this configuration of layers, where the soft-magnetic film is $Ni_{80}Co_{20}$, is shown as Fig. 51.14b. The units of the coupling constant are memu/cm^2 (×10 A in SI units) (coupling per unit of film area). The coupling constant can be either antiferromagnetic ($J_{12} < 0$) or ferromagnetic ($J_{12} > 0$) and can have a magnitude varying between +25 to −75 memu/cm^2 (+250 to −750 A). By varying the thickness of the Co layer it is possible to adjust the total magnetic field at the layer F_{II} to be zero.

Table 51.2 Comparison of alternative antiferromagnetic films for transverse bias of Permalloy films

Property	NiFe/FeMn [51.25]	NiFe/NiMn [51.25]	NiO/NiFe [51.25]	CoNiO/NiFe [51.26]	NiFe/IrMn [51.26]	NiFe/CrMnPt [51.27]	NiFe/Pd−Pt−Mn [51.28]
Corrosion resistance	Low	High	Very high	Excellent	Moderate	Good	High
Coupling field H_{ua}Oe (kA/m)	≈ 77 (6.12)	≈ 206 (16.4)	≈ 46 (3.66)	≈ 45 (3.58)	60 (4.77)	≈ 350 (27.84)	$(Pd_{0.6}Pt_{0.4})_{0.5}Mn_{0.5}$ 80 (6.36)
Coercivity H_{ua} Oe (kA/m)	≈ 6 (0.48)	≈ 116 (9.23)	≈ 35 (2.78)	11 (0.88)	8 (0.64)	≈ 23 (1.82)	16 (1.27)
Blocking temperature (°C)	≈ 150	≥ 450	≈ 200	150	250	320	300
Annealing	Not required	Required	Not required	Not required	Not required	Required	Required

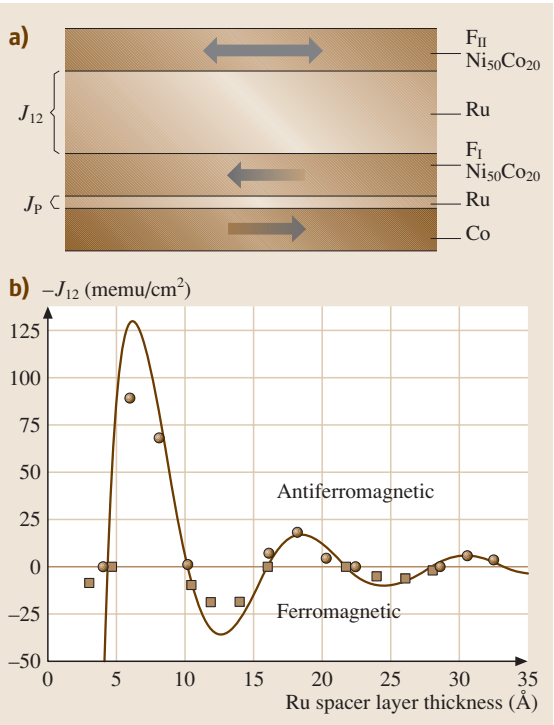

Fig. 51.14 **(a)** Geometry of ferromagnetic films coupled by thin layers of ruthenium. **(b)** Magnetic coupling constant per unit of film area between layers F_I and F_{II} of the films shown in **(a)** versus the thickness of the ruthenium layer. (After [51.29])

An overall spin valve consists of a sequence of thin films such as: MnFe 21 Å/Co 30 Å/Ru 7 Å/Co 30 Å/Cu 25 Å/Co 30 Å/$Ni_{80}Fe_{20}$ 28 Å, where the first four films (MnFe/Co/Ru/Co) form a *synthetic antiferromagnetic* film since the final Co film of these four films is pinned to a direction opposite to that for the first Co film. This Co film then acts as a pinned film in a spin valve together with the final three films (Cu, Co, and $Ni_{80}Fe_{20}$). The thickness of ruthenium listed in the sequence of films is optimum for antiferromagnetic coupling between the Co films. The last Co film is a nanolayer, which increases the magnetoresistive coefficient, as we have discussed [51.23]. The advantages of the synthetic antiferromagnet for pinning the pinned film compared with just an antiferromagnetic film (e.g., FeMn, NiO, NiMn or IrMn) are

1. the pinning coupling field is an order-of-magnitude larger, and
2. the magnetostatic coupling field from the pinned layer to the free layer is reduced. The magnetostatic coupling field is reduced since the two Co films in the synthetic antiferromagnet are antiferromagnetically coupled and hence their magnetostatic fields at the free film cancel. The synthetic antiferromagnet contributes to ensuring that the only magnetic field at the free film is that from the transitions in the recording medium.

One last requirement for the proper operation of the spin valve is that there is abutted on the two ends of the structure a permanent magnetic film referred to as the *hard bias* film (discussed in [51.4]). The permanent magnetic films are similar to the cobalt alloy magnetic films used for disk recording surfaces (to be discussed). The purpose of the hard bias is to reduce the presence of magnetic domains in the free film and to reduce Barkhausen jumps of the domain walls in the presence of the exter-

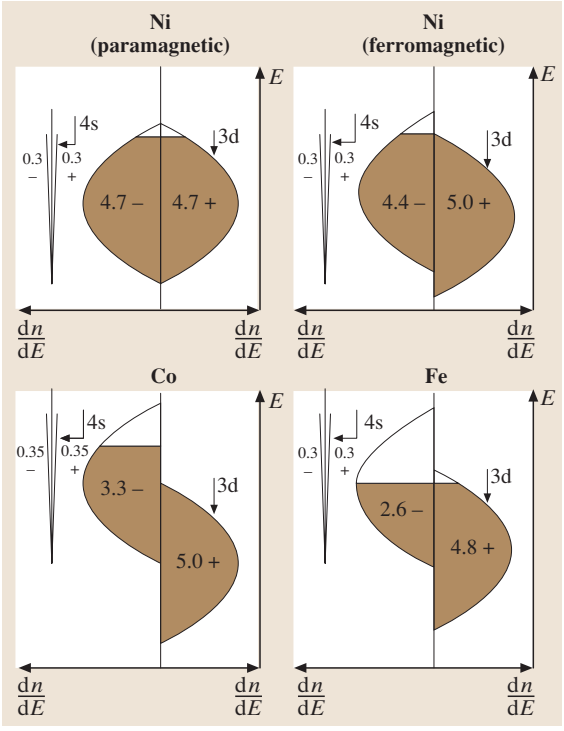

Fig. 51.15 Schematic of density of states curves for the ferromagnetic transition elements (Ni, Co and Fe). Both the 4s and 3d bands are shown. The magnetization of the elements is due to the difference between the spins in the spin-up and spin-down bands and the bands are full of electrons to the Fermi level (the shaded region). (After [51.30])

nal magnetic fields from the transitions in the recording medium.

The stack of films used in a spin valve has been discussed. The films used in Fig. 51.10, which we used to illustrate the GMR effect in a $Co_{90}Fe_{10}/Ni_{80}Fe_{20}$ free film, was: Ta (50 Å)/$Ni_{80}Fe_{20}$ (60 Å)/$Co_{90}Fe_{10}$ (55 Å)/Cu (variable)/$Co_{90}Fe_{10}$ (55 Å)/FeMn (100 Å)/Ta (70 Å) [51.20]. In this case the antiferromagnetic film was FeMn (typically about 50%, 50%) and the Ta films are used to protect the rest of the stack.

Origin of GMR

The physical origin of the GMR effect lies in the differential scattering of electrons with spins in the same direction as the local magnetization (spin-up electrons) or opposite to this direction (spin-down electrons) at the interfaces and in the bulk part of the thin films comprising the GMR stack of films. The ferromagnetic transition elements (Fe, Co and Ni) have different 3d band structures, as shown in Fig. 51.15 [51.30] and discussed by [51.4]. This figure illustrates the energy of electrons in the two half-bands for spin-up and spin-down electrons versus the density of states $D(E)$ (number of states per unit energy per unit volume) in the 3d band for the ferromagnetic transition metals. The 4s bands are also shown. Electrons in the 4s bands make only a small contribution to the net spin but, because of the larger mobility (inversely proportional to the curvature of the bands), they are largely responsible for the current. The bands are filled to the Fermi energy at 0 K, and states above, but close to, the Fermi level are occupied at room temperature (illustrated by the shaded region in Fig. 51.15). The conductivity of a metal is given by

$$\sigma = \frac{1}{3} e^2 v_F^2 \tau D(E_F) ,$$

where e is the electron charge, v_F is the velocity of electrons at the Fermi energy, τ is the mean scattering time and $D(E_F)$ is the density of states at the Fermi energy [51.31]. If the mean scattering time (τ) is held constant then it is seen that the conductivity increases with the density of states at the Fermi energy; however, the scattering of the 4s electrons with a given spin is large when there are a large number of scattering centers and empty states with the same spin in the 3d band, i. e., the density of states at the Fermi energy $D(E_F)$ in the 3d band is large. In the ferromagnetic transition metals this is the larger effect and

$$\rho \propto D(E_F) .$$

The scattering is due to spin–spin scattering, and spin–orbit scattering is believed to be small [51.32, 33]. The

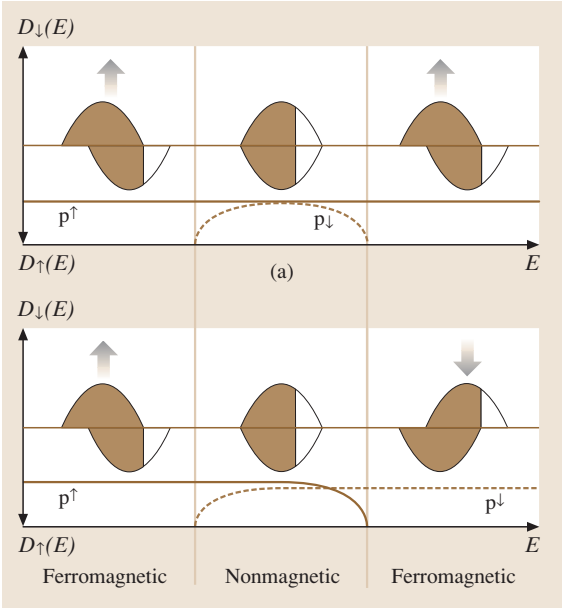

Fig. 51.16 Density of states curves for the spin valve structure in the ferromagnetic spin configuration (*top figure*) and the antiferromagnetic spin configuration (*bottom figure*). The resistivities of the layers are shown on the bottom part of the figures. (After [51.30])

magnetic moment per atom can be deduced as the difference in the number of electrons/atom with spin-up (the majority) versus those with spin-down. For example, the magnetic moment per atom for iron is 4.8 – 2.6 = 2.2 Bohr magnetons per atom. From Fig. 51.15 we conclude that the differential scattering will be large in cobalt since for this element the difference in the density of states at the Fermi level is large [approximately 8–10 to 1 [51.30]]. A schematic of the density of states versus energy for the three films comprising the spin valve structure from the two extreme cases of the orientation of the ferromagnetic films (ferromagnetic configuration and antiferromagnetic configuration) is shown in Fig. 51.16 [51.30, 34]. All films have the same Fermi energy. Mathon described the GMR effect by discussing the differential scattering of *holes* in the 3d bands, but by concentrating on the scattering of electrons from the 4s to the 3d band we can make the same conclusions [51.32, 34]. It is assumed that the mean free path for the electrons is large compared with the thickness of any layer in the superlattice. Consider the ferromagnetic configuration case (top of Fig. 51.16): here the majority electrons have spin-up and the scattering of 4s electrons is low in both ferromagnetic films since both have a low

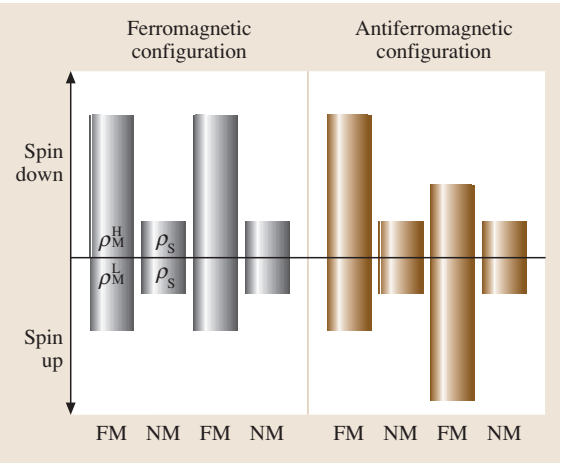

Fig. 51.17 Distributions of local resistivities for the spin-up and spin-down electrons in the ferromagnetic and antiferromagnetic spin configurations. (After [51.30])

density of states at the Fermi level. The nonmagnetic film has a larger density of states and will scatter electrons regardless of the orientation of the ferromagnetic films, which is why this film must be thin. Now consider the antiferromagnetic configuration case in Fig. 51.16: from the density of states at the Fermi level in the three films it is seen that the scattering is large in the right-hand ferromagnetic film for the electrons leaving the left-hand ferromagnetic film with spin-up (top density-of-states curve), resulting in large resistivity for this class of electrons. Similarly, the scattering of spin-down electrons is large for the left-hand ferromagnetic film. The

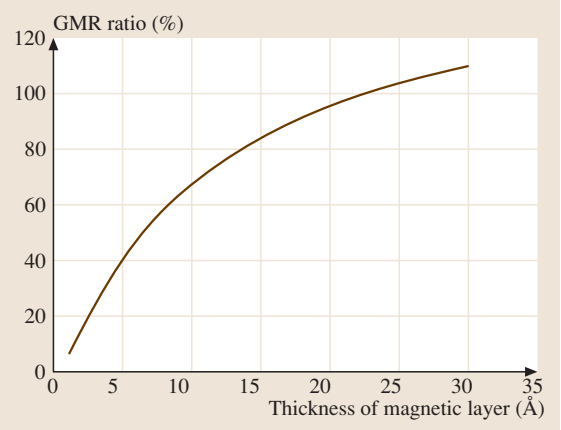

Fig. 51.18 $\Delta R/R$ versus the thickness of the magnetic layer (M) for a nonmagnetic layer thickness (N) of 10 Å for a Co/Cu spin valve. (After [51.30])

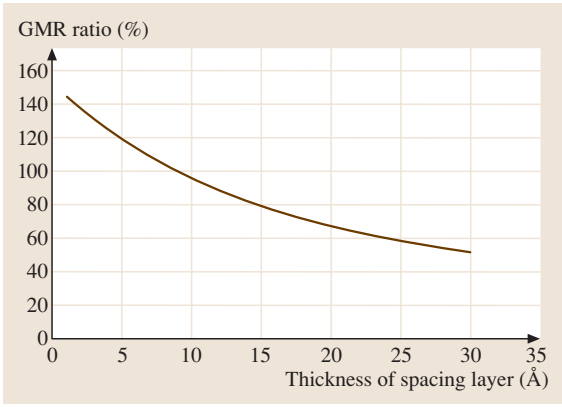

Fig. 51.19 $\Delta R/R$ versus the thickness of the nonmagnetic layer (N) for a magnetic layer thickness (M) of 20 Å for a Co/Cu spin valve. (After [51.30])

resistivity for the spin-up and spin-down electrons for the three films [ferromagnetic (FM), nonmagnetic (NM) and ferromagnetic (FM)] in the ferromagnetic and antiferromagnetic orientation cases is shown as a schematic in Fig. 51.17 [51.30] where it is shown that the ferromagnetic orientation of the ferromagnetic films has a (relatively) low resistivity path for the spin-up electrons while the resistivity for the antiferromagnetic orientation of the ferromagnetic films is high for both spin-up and spin-down electrons.

The change in resistance of the spin valve structure can be analyzed in terms of the different resistivities for the ferromagnetic and antiferromagnetic orientation of the two ferromagnetic films shown in Fig. 51.16 [51.30]

$$\frac{\Delta R_{\max}}{R_0} = (\alpha-\beta)^2 \Big/ \left[4\left(\alpha + t_{\text{nonmagnetic}}/t_{\text{magnetic}}\right) \times \left(\beta + t_{\text{nonmagnetic}}/t_{\text{magnetic}}\right)\right] , \quad (51.12)$$

where

$$\alpha = \frac{\rho_M^H}{\rho_S} , \quad \beta = \frac{\rho_M^L}{\rho_S} ,$$

where $t_{\text{nonmagnetic}}$ is the thickness of the nonmagnetic film and t_{magnetic} is the thickness of the magnetic film.

Figure 51.18 shows the variation of $\Delta R_{\max}/R_0$ for $t_{\text{nonmagnetic}} = 10$ Å versus t_{magnetic} for assumed values of $\alpha = 8.0$ and $\beta = 1.0$, which is appropriate for a Co/Cu superlattice [51.30]. For thicknesses of the magnetic films beyond approximately 10 Å, the change in $\Delta R/R$ decreases. Figure 51.19 shows the variation of $\Delta R/R$ for $t_{\text{magnetic}} = 20$ Å versus $t_{\text{nonmagnetic}}$. The decrease in

$\Delta R/R$ is rapid with increasing thickness of the nonmagnetic layer. This combination of films is not used in spin valves since the cobalt film is not magnetically soft; the usual choice is Permalloy with a variety of nonmagnetic transition metals and the resulting $\Delta R/R$ is lower.

51.1.4 Longitudinal Recording Media

Magnetic recording media used in modern disk drives are all sputter-deposited thin films of cobalt alloys for high coercivity and media flux ($M_r \times \delta$). Coercivities of 4000–5000 Oe are used (2006) and are limited by the ability of the write head to record on the media. The alloys that have evolved are four- or five-element alloys of CoPtCrX, where X is Ta or B or both. A typical atomic concentration of the four-element media is $Co_{64}Cr_{24}Pt_8B_4$. It has been found necessary to form a microstructure in the magnetic film that consists of a phase of small magnetic grains isolated by a nonmagnetic phase. The isolation of the magnetic grains results in less exchange coupling between grains and reduced noise – as we will discuss. Chemical segregation of $Co_{100-x}Cr_x$ alloys forms a nonmagnetic phase (Cr-rich) and a magnetic phase (Co-rich) and the nonmagnetic phase forms at the grain boundaries. The microstructure is controlled by undercoats that promote grain growth with the axes of the grains in the plane of the film. Platinum results in higher crystalline anisotropy and boron promotes the formation of an amorphous alloy of CoCrB, which grows at the grain boundaries, further reducing the exchange coupling. Figure 51.20 shows the microstructure for a magnetic recording surface, illustrating the separation of the grains by the amorphous CoCr phase and, in the lower image, the c-axis stacking of the hcp grains [51.35]. In five-element alloys [CoCrPtBTa], Ta assists the segregation of Cr at the grain boundaries [51.36]. Some recording media use as many as three magnetic layers with the saturation magnetization increasing towards the read head, so that the average saturation magnetization is reduced while the magnetization nearest to the read head is increased. The layer of films comprising a recording layer at the areal densities for a 130-Gb/in^2 demonstration were: NiP-plated aluminium substrate with mechanical texturing in the data-recording zone/Cr seed layer/a CrMoX (X = grain-boundary segregation-enhancement element) underlayer/a CoCrT intermediate layer/two ferromagnetic layers (one with high Cr/low B concentration and the second with low Cr/high B concentration) and a double-layer amorphous carbon overcoat [51.37]. The substrate used for the samples in Fig. 51.20 was glass. Glass substrates have several advantages over aluminium with electroless Ni(P) (for hardness) substrates, including increased stiffness, which leads to reduced flutter, increased hardness and reduced susceptibility to corrosion. However, aluminium substrates continue to be used in nonportable applications because of reduced cost. The amorphous carbon is required to protect the magnetic film and to give a mechanically rigid surface on which the slider can fly at less than 25 nm.

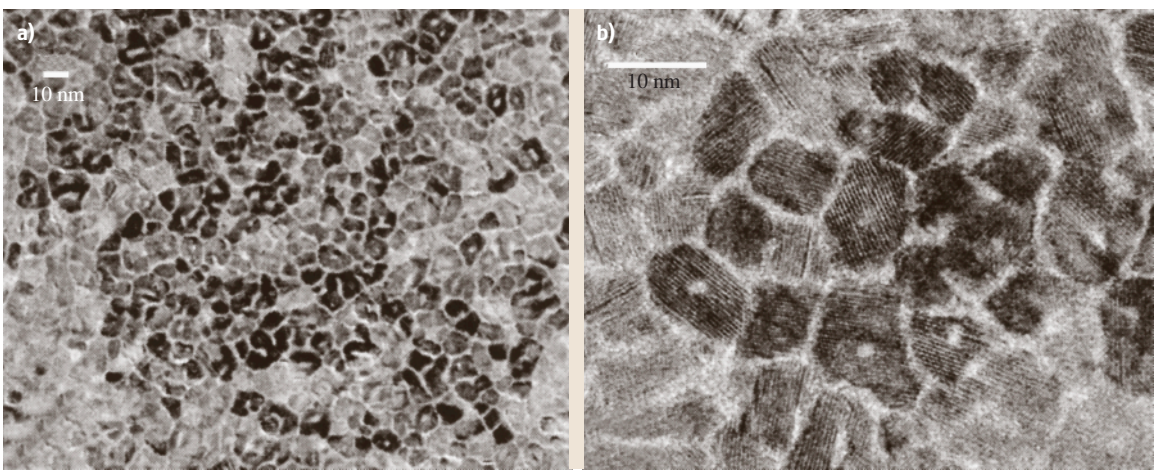

Fig. 51.20a,b Plan-view electron microscope images [the upper image **(a)** is lower resolution and the lower **(b)** is higher resolution] of the CoPtCrB magnetic alloy layer used in the 35-Gb/in^2 demonstration by IBM. The amorphous grain boundaries are seen as white and the c-axis stacking of the hcp grains can be seen within the grains in the higher-resolution image. (After [51.35].) The images were taken by Kai Tsang of IBM

Media Noise

In modern digital recording systems the dominant noise voltage which appears simultaneously with the desired read signal at the terminals of the read head is that from the recording media, assuming that the resistance from the read head is not excessive. Noise in the read channel is caused by random variations in the location of the recorded transitions. Transitions are not straight across the recorded track, as we assumed in our discussion of the transition parameter, but instead form zig-zag patterns in order to reduce the large demagnetizing field and demagnetizing energy associated with the longitudinal transition (discussed in [51.4]). Transitions also tend to follow the grain boundaries in the polycrystalline media. To achieve low media noise, it is required to have a small grain size so that the random nature of the grains is averaged over the width of the read head (the track width). An analysis of the signal-to-noise ratio, defined as the base-to-peak signal voltage amplitude (S_0) over the media noise voltage amplitude (N) has been published [51.24]

$$\left(\frac{S_0}{N}\right)^2 = 0.31\left(\frac{B}{a}\right)^2\left(\frac{PW_{50}}{B}\right)\frac{W_r}{W_c}\,, \qquad (51.13)$$

W_r: width of read head,
PW_{50}: width of the read pulse at 50% of the peak amplitude,
W_c: cross-track correlation width, which has been approximated as the grain or cluster size of the recording media. The grain size is a distribution and W_c is the mean of the distribution,
a: transition parameter discussed above,
B: length between bits.

For a reliable low error rate the value of $20\log S_0/N$ is required to be above 26–27 dB and this has required an increasingly smaller grain size as the width of the read head has decreased, resulting in higher track densities. For a 10-Gb/in^2 system the value of W_r was 0.505 μm and the required mean of the grain size was 12 nm [51.38]. The ratio B/a has been ≈ 3 to avoid severe distortion of the transition across the track, referred to as percolation (discussed in [51.4]) and the ratio PW_{50}/B has been in the region 2.5–2.8 for the type of detection channels used in present disk drives [partial response maximum likelihood (PRML)]. Therefore, to maintain constant S_0/N the ratio of the track width to the grain size must be kept constant and, with the decreased track width, the grain size must decrease in proportion.

Increased areal density has required decreased mean grain size but, equally important, tighter distributions of grain size. The distributions are closely matched by log-normal distributions of the form

$$y = \frac{1}{\sigma_Z\sqrt{2\pi}}\exp\left(-\frac{(Z-\overline{Z})^2}{2\sigma_Z^2}\right)\,, \qquad (51.14)$$

where Z is the $\log_{10}$ value of the grain diameter, $\overline{Z}$ is the mean value of Z and σ_Z is the standard deviation of Z. Grain size distributions are measured on foils by tunneling electron microscopy (TEM). Figure 51.20 showed the microstructure of a typical recording surface, emphasizing the segregation of the grains by the nonmagnetic constituents of the alloy. The distribution of the grain sizes in recording media for 20 GB/platter (counting both sides of the platter) and the higher density 80 GB/platter are shown in Table 51.3 [51.17]. Both the mean and standard deviation for the 80 GB/platter are reduced from those of the 20 GB/platter media. We will discuss the decay rates shown in Table 51.3 in the next section. The trend in the mean grain size and grains

Table 51.3 Comparison of 20- and 80-GB/platter disk characteristics (after [51.17])

	20 GB/ 90 mm disk	80 GB/ 90 mm disk
H_c (Oe)	2700	4200
$M_r\delta$ (memu/cm^2)	0.46	0.32
Average grain size (nm)	10.8	9.1
Distribution sigma	0.41	0.24
Amplitude decay rate (%/decade)	0.7	0.4

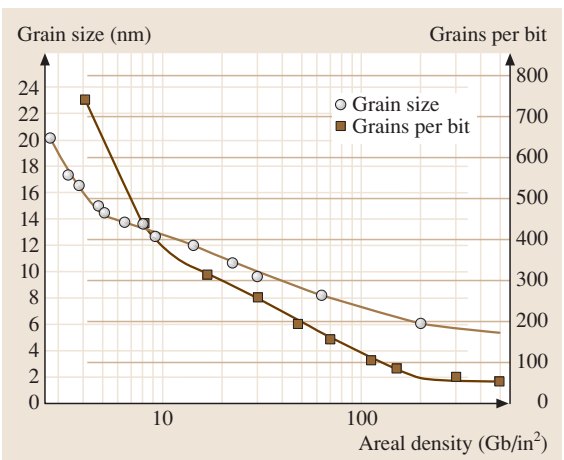

Fig. 51.21 Grain size and grains/bit for sputtered cobalt alloys as a function of areal density in Gb/in^2. (After [51.17])

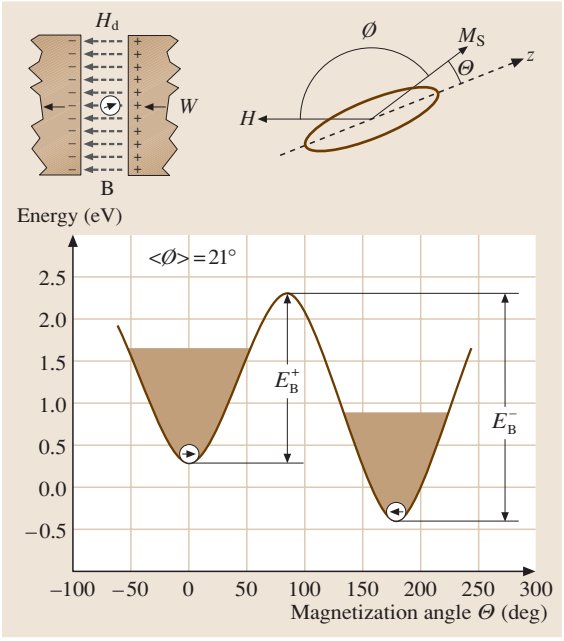

Fig. 51.22 Calculated energy of an isolated single-domain particle at the center of an 80-nm-long dibit transition. The properties of the particle are listed in Table 51.4. The ratio of the barrier height to thermal energy is 43 (see text) and the height 43 $k_B T$ is shown shaded. There is margin between the top of the shaded region and E_B^+ and the particle is stable for the time t_x of 10 y. (After [51.39])

per bit for recording films versus areal density is shown in Fig. 51.21 [51.17]. A serious problem with this trend is the fact that the ratio of magnetic to nonmagnetic volume in the film is decreasing faster than the average grain size, which results in the number of grains per bit decreasing faster than the average grain size. The price to be paid for the increasingly small grain size is the stability of the recorded data over time as we discuss in the next section. To investigate how far the areal density can be extended with longitudinal recording use has been made of the signal-to-noise ratio calculation to see if an areal density of 200 Gb/in^2 is feasible. To ensure that the signal-to-noise ratio does not degrade when extending the areal density from 60 to 200 Gb/in^2, it is required that: (a) the transition parameter be reduced from 12.8 to 6.2 nm, to achieve which the coercive field (H_c) must be increased from 4000 to 5000 Oe, and (b) the product of the magnetization and thickness ($M_r\delta$) be reduced from 0.32 to 0.2 memu/cm^3. In addition, the head–medium spacing must be reduced from 30 to 15 nm [51.17].

Superparamagnetic Effect

To maintain the growth in areal density as shown in Fig. 51.1, it is necessary to reduce the physical dimensions of the recording-system components — and, to maintain the signal-to-noise ratio at levels required for satisfactory error rates, this includes reducing the mean grain size of the recording media. However, at some grain size the thermally driven fluctuations of the orientation of the magnetization in the isolated grains result in increased probability of the magnetization being switched from the desired orientation, as initially recorded, to the opposite direction. This instability of the magnetization is the *superparamagnetic effect*. The magnetic energy in an isolated grain is $K_u V$, where K_u is the uniaxial anisotropy consisting of crystalline, magnetostriction and shape contributions and V is the volume of the particle or grain with diameter D [$\pi(D/2)^2\delta$]. Thermal energy supplied from the environment to the particle is $k_B T$, where k_B is the Boltzmann constant (0.8619×10^{-4} eV/K). An analysis of the superparamagnetic effect using an isolated small single-domain asymmetrical particle is summarized in Fig. 51.22 [51.39]. Here, the magnetic particle is assumed to be in the center of two transitions and the energy contour results from an analysis using only

Table 51.4 Energy of single-domain particle in magnetic field of two transitions (after [51.39])

Parameter	Value
B (dibit length)	80 nm
K_u (particle anisotropy energy, consisting of shape and crystalline anisotropy contributions)	1.5×10^6 erg/cm^3 (1.5×10^5 J/m^3)
$M_r\delta$	0.39 memu/cm^2 (3.9 mA)
M_S	375 emu/cm^3 (375×10^3 A/m)
D (grain or particle diameter)	15 nm
δ (media thickness)	13 nm
V (grain or particle volume)	$\pi\times(D/2)^2\times\delta$
H_d (demagnetizing field between transitions)	780 Oe (62 kA/m)
$\langle\phi\rangle$ (mean angle of field with respect to grain or particle axis)	21°

shape and crystalline anisotropy (combined into K_u) and magnetostatic energy terms.

$$E(\theta, \phi) = K_u V \sin^2 \theta + HM_s \cos(\theta - \phi) \ . \quad (51.15)$$

It is assumed in Fig. 51.22 that the angle ϕ has a mean value $\langle\phi\rangle = 21°$. The energy contour shown in Fig. 51.22 results from the application of (51.15) with the parameters listed in Table 51.4. The energy required to switch the particle from the initially magnetized direction is shown as E_B^+. In the absence of an external or demagnetizing field, the energy barrier is

$$E_B^+ = K_u V \ .$$

With a demagnetizing field (H_d) the switching field is reduced since the field is in the direction of the switched magnetization

$$E_B^+ = K_u V \left(1 - \frac{|H_d|}{H_0}\right)^{1/2} \ . \quad (51.16)$$

With a random two-dimensional (2-D) system $H_0 = 2K_u/M_s$. The magnetization of the particle will switch when $H_0 = H_d$. When the magnetization of the particle is switched, the new energy barrier is E_B^- and is increased in depth since the demagnetizing field is now in the same direction as the magnetization. Using the set of parameters listed in Table 51.4, the depth of E_B^+ [with a demagnetizing field of 780 Oe (62 kA/m)] is approximately 1.9 eV.

The time constant for the thermally driven switching of the magnetic particle in the presence of a magnetic field, which in the case under consideration is the demagnetizing field acting on the magnetic particle, can be found using an Arrehenius–Néel model

$$\tau = \tau_0 \exp\left(\frac{-E_B^+(H)}{k_B T}\right) \ ,$$

where $\tau_0 = 1/f_0$ and f_0 is an *attempt frequency*, usually taken as $\approx 10^9$ Hz [51.39]. The energy barrier depends on the thermal energy and the fraction x ($0 < x < 1$) of the retained magnetization and the storage time t_x

$$E_B^+(H) = \ln\left(\frac{t_x f_0}{|\ln x|}\right) k_B T \ ,$$

$$t_x = |\ln x|\,(\tau_0) \exp\left(\frac{E_B^+(H)}{k_B T}\right) \ . \quad (51.17)$$

As an example, if the required storage time is $\approx 10^8$ s (10y) and the percentage loss of data amplitude is 5%, then $x = 0.95$ and $|\ln 0.95| = 0.05$ and

$$\frac{E_B(H)}{k_B T} \cong 43 \ .$$

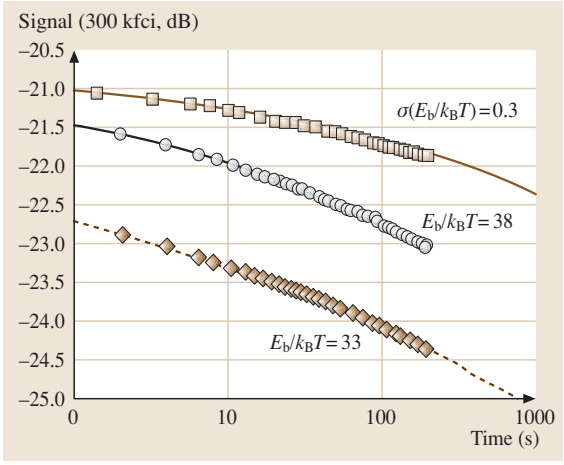

Fig. 51.23 Signal loss versus time at room temperature and 300 k flux changes per inch for three magnetic recording surfaces: The first two (*from the top*) are SFM or AFC media with layer thicknesses of: [12 nm/0.7 nm/4 nm] (*open square*), [12 nm/1.4 nm/4 nm] (*open circle*). The *lower curve* is for a 12-nm single layer (*solid diamond*). (After [51.40])

The thermal energy $k_B T$ at 350 K (the assumed operating temperature of a typical disk drive) is 0.03 eV, $43 \times k_B T \approx 1.25$ eV and the shaded region in Fig. 51.22 has this energy level. Since there is some margin between the thermally driven contribution to switching and the top of the barrier, the particle is stable (over the -10–*year* period). However, for smaller volumes (V) the value of E_B^+ decreases and the particle could become unstable. For example, if the thickness of the recording media is reduced from that assumed in Fig. 51.22 (13 nm) to 6 nm, the value of E_B^+ is reduced to ≈ 0.9 eV and the thermal energy would easily switch the particle.

A dramatic loss of data over time is observed with recording media with media flux ($M_r \times \delta$) less than about 0.25 memu/cm^2. Figure 51.23 shows amplitude loss of recorded data for three different media at a linear density of 300 kΛux changes per inch at room temperature [51.40]. The three media are: a single-layer of CoCrPtB (lowest curve with a thickness of 12 nm); and two recording surfaces we will discuss in the next section. The signal decay rate R is defined as

$$R(H_d, T) = 100 \frac{\frac{A(t)}{A(t_0)} - 1}{\log(t/t_0)} \ , \quad (51.18)$$

where the signal amplitude of a square-wave pattern is $A(t)$. With $t_0 = 1$ s, the decay rate per decade for the media shown as the lower curve in Fig. 51.23 is

found to be −7.19%. The decay rate for the other media will be discussed in the next section. The decay rates for the two recording films shown in Table 51.3 are −0.7%/decade and −0.4%/decade for the 20 GB/platter and 80 GB/platter media, respectively. In a conventional disk recording system this superparamagnetic effect was judged to limit the areal density to somewhere in the range 36–100 Gb/in^2 (reviewed in [51.39]). The superparamagnetic effect and the requirement for low media noise result in recording-system designers being caught in two inconsistent requirements: first, a small grain size for the recording media is required for adequate signal-to-noise ratio, so that the number of grains per bit remains constant (51.13), and second, a large grain size is required for small data loss over time because of the superparamagnetic effect [(51.16) and (51.17)]. The requirement to reduce the thickness of the recording media can be deduced from the need for low values of $M_r\delta$ for short transition lengths (51.5). The approach of increasing the anisotropy of the grains to increase K_uV to resolving the superparamagnetic effect is limited by the ability of write heads to record on the media with the resulting increased media coercivity. The present values of areal density are approaching this limit. However, as can be seen from Table 51.3, the decay rates observed with the smaller grain size–higher density media is actually smaller than that for the larger grain size–lower density media. A possible explanation is that the K_uV values for the smaller grains are higher than for the larger grains [51.17]. In the next section we discuss a novel approach that has extended the progression in areal density.

Antiferromagnetically Coupled (AFC) or Synthetic Ferrimagnetic (SFM) Media

The invention of a new form of recording media which has decreased the impact of the superparamagnetic effect was accomplished simultaneously by teams of researchers at the Fujitsu and IBM Almaden Research Laboratories [51.41, 42]. The new form of recording media consists of two ferromagnetic layers coupled by a thin layer of ruthenium [antiferromagnetically coupled (AFC) or synthetic ferromagnetic media (SFM)], which results in an antiferromagnetic coupling of the two films, similar to that used in the spin valve for a synthetic antiferromagnet. In order for the coupling between the two ferromagnetic layers to be antiferromagnetic, the thickness of the ruthenium layer, referred to by IBM as "pixie dust", is required to be approximately 0.6 nm [51.42]. A schematic of the antiferromagnetic coupled media and the resulting hysteresis curve is shown as Fig. 51.24 [51.40]. The sharp reduction in the remanent magnetization at ≈ 80 Oe is due to the switching of the thinner lower layer (M_rt_2) and the lowered value of the remanence is advantageous for reduced transition noise and transition length. The curve with solid circles is a remanence hysteresis curve measured by subjecting the sample to a negative reversing field and then increasing the field in a positive direction to zero and plotting the remanent magnetization. This measurement is an attempt to simulate what happens when a recording medium leaves the vicinity of the recording head. By analyzing the read pulse from the transition in the upper layer combined with the read pulse from the transition with reversed sign from the lower layer (the layers are antiferromagnetically coupled), it can be shown that no degradation of the resolution (PW_{50}) of the system results from having two as opposed to one recording layer [51.42]. The advantage of the AFC or SFM configuration is that the medium is in fact thicker than would be required for the given recording density using a single

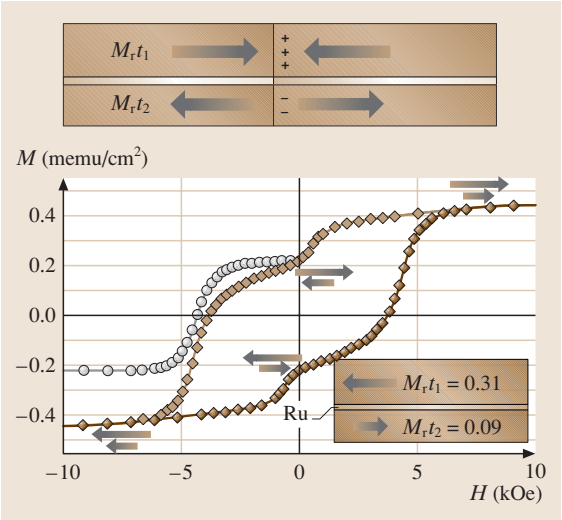

Fig. 51.24 (*top*) Schematic of the antiferromagnetically coupled (SFM or AFC) media showing the two ferromagnetic layers coupled by a thin layer of ruthenium ('pixie dust') and with a single magnetic transition for which the magnetizations in the two layers are oppositely directed. (*bottom*) Magnetic hysteresis curve for the SFM or AFC media with remanent thickness products for the two ferromagnetic layers shown in the *inset* and measured at 350 K. The *filled triangles* are the major hysteresis curve and the *filled circles* are the remanence hysteresis curve. The *arrows* show the directions of the magnetization in the two films. (After [51.40])

layer and hence is less susceptible to the superparamagnetic effect (51.17). The effective volume is bounded by

$$K_u V_1 < K_u V_{eff} < K_u V_1 + K_u V_2$$

and with tight coupling and alignment of the axes of the grains the upper limit is approached. The effective remanent magnetization × thickness product is close to

$$M_r t_1 - M_r t_2$$

and this reduces the pulse width over that a single-layer recording medium (51.10).

Because of the antiferromagnetic coupling, an exchange magnetic field $H_{ex,2}$ acts on the lower magnetic film

$$H_{ex,2} = \frac{J_{ex,2}}{M_2 t_2}$$

and a typical value for the antiferromagnetic exchange constant $J_{ex,2}$ is $0.06\,\mathrm{erg/cm^3}$ ($6\,\mathrm{mJ/m^3}$) [51.44]. For the magnetization of the lower layer to assume the opposite direction to that of the top layer before the field H is reduced to zero, it is required that $H_{ex,2} > H_{c2}$. The antiferromagnetic exchange constant can be increased by adding a thin layers of cobalt or cobalt alloys known as E layers to both sides of the ruthenium layer [51.43]. The increase in the antiferromagnetic exchange constant is rapid with thickness of the E layers and we show in Table 51.5 a listing of J_{ex} for several E layers [51.43]. The largest increase in J_{ex} is with cobalt, but this material suffers from significant degradation on overwrite and poor signal-to-noise ratio compared with cobalt alloys.

To illustrate that the AFM or SFM media configuration actually results in reduced amplitude loss over time, we show in Fig. 51.23 the amplitude loss with two SFM media: 12/0.7/4 (open squares) and 12/1.4/4 (open circles), where the numbers are the thickness of the three layers in nm and the value of E_B/k_BT is 38 [51.40]. The signal decay rate is −4.14% per decade for the top curve (open squares) and −6.45% per decade for the middle curve (open circles) [51.40]. The coupling between the two magnetic films is antiferromagnetic for the top curve and ferromagnetic for the middle curve and the lower curve is a single magnetic layer. The AFM or SFM media clearly reduces the decay rate. The improvement is even more significant with a larger value for E_B/k_BT and values of R less than 1%/decade with $M_r t$ values lower than $0.2\,\mathrm{memu/cm^2}$ have been reported by IBM researchers using static magnetization measurements with a reversing magnetic field to mimic the demagnetizing field [51.42]. AFM media are being used in IBM portable disk-drive applications [51.45]. Areal densities larger than $100\,\mathrm{Gb/in^2}$ have been reported with longitudinal recording using AFM media [51.46]. The magnetic recording layers were alloys of CoCrPtB with an average grain size of 9.4 nm. The write head was trimmed on the air-bearing surface to the final track width using a focused ion beam and the track density was 149 ktracks/in and the bit density was 720 kbits/in [51.46].

The data shown in Table 51.3 also shows that it is possible to achieve low decay rates with single recording layers [51.17]. Analysis comparing SAF and single-layer media has shown that the single-layer media is preferred unless the media flux drops below about $0.25\,\mathrm{memu/cm^2}$ with H_c values constrained below 4300 Oe. If recording heads are able to record with adequate overwrite on media with coercivity greater 4300 Oe, then the single-layer media is preferred [51.47].

Dynamic Coercivity

Another manifestation of thermal effects on magnetic properties is a change in coercivity with switching time. With long periods of time the probability that a particle will switch is increased by thermal excitation and with short periods this probability is decreased – leading to a change in the coercivity of the particle. An experimental study of this effect was done on a test stand in which a stationary write head is driven by a current pulse of variable duration over a previously magnetically saturated recording medium. The current pulse records two transitions (a dibit). The width of each transition is essentially the gap of the write head and the length of

Table 51.5 Comparison of materials for E layers: J_{ex} values and degradation in overwrite and signal to media noise (after [51.43])

Material for E layers (all 1 nm thick)	Co	Co–Cr	Co–Cr–X
J_{ex} ($\mathrm{erg/cm^2}$)	0.73	0.59	0.24
Degradation in overwrite (dB) with respect to SFM media without E layers (negative values indicate improved overwrite)	10	≈ 3	≈ −6
Degradation in S/N_m (dB) with respect to SFM media without E layers	≈ 4.5	≈ 1.6	≈ 1.5

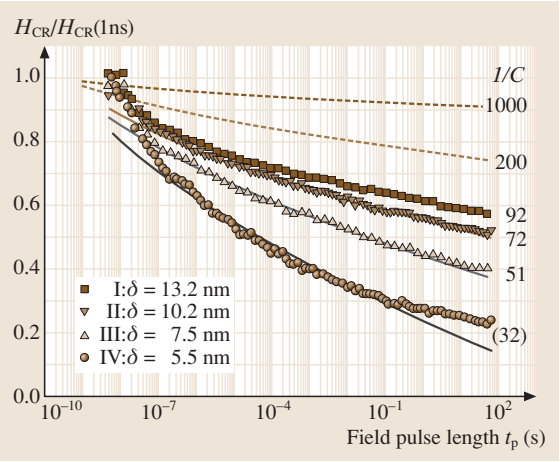

Fig. 51.25 Dynamic coercivity $H_{CR}(t)$ for a series of $Co_{64}Pt_{14}Cr_{22}$ films with variable thickness. (After [51.39])

the reversed magnetization region varies with the pulse width (t_p). The dibit is read with a magnetoresistive sensor moved across the recorded transitions resulting in a dibit pulse. By measuring the amplitude of the dibit signal as a function of the pulse width and varying the magnitude of the reverse field and measuring H_{head} (I) it is possible to deduce the remanent coercivity (H_{CR}) as a function of t_p. The resulting curves of H_{CR}/H_{CR} (1 ns) are shown in Fig. 51.25 [51.39]. The experimental slopes C increase as the thickness decreases. The inverse slope parameter is given by

$$\frac{1}{C} \cong \frac{K_u V}{k_B T} ,$$

which is the superparamagnetic stability parameter discussed above and it is observed that, even with a stability factor larger than 51, for which the superparamagnetic region is avoided, the coercivity increases significantly for short switching times. This is the actual coercivity that must be exceeded by the write-head magnetic fields to switch a recording film.

51.1.5 Perpendicular Recording

The technology that is now starting to supplant longitudinal recording is perpendicular recording. Perpendicular recording offers a way out of the conundrum caused by the need for thinner recording media for improvements in recording density and the need for larger particles to reduce the impact of superparamagnetism. In perpendicular recording the magnetization in the recording media is held perpendicular to the surface

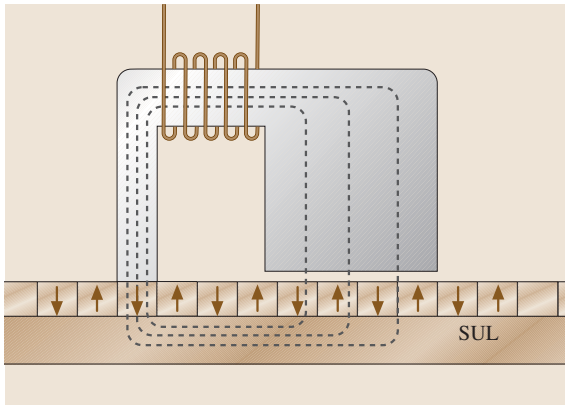

Fig. 51.26 Schematic of a perpendicular recording system. (After [51.4])

of the recording media by a perpendicular anisotropy large enough to overcome the large demagnetizing field with this orientation of the magnetization. A schematic of a perpendicular recording system including a probe write element and a magnetically soft underlayer (SUL) is shown as Fig. 51.26. It is also possible to have a perpendicular recording system with a ring write head and a single-layer media, but this approach has not been developed. In contrast to longitudinal magnetic recording the SUL is required for a low-reluctance path for the magnetic flux generated by the coil on the write element. One advantage of perpendicular recording is that the magnetic field for recording is larger than that for longitudinal recording since the magnetic field from the write pole is in the gap of the write head, in contrast to longitudinal recording where the field leaks from the write gap. A schematic of the total geometry for longitudinal and perpendicular recording is shown in Fig. 51.27 [51.1]. Reading for perpendicular recording is accomplished with a GMR sensor as with longitudinal recording. The major difference in the write head is that it uses a single pole to generate the perpendicular magnetic field with a wider (to reduce the reluctance) return pole. The write head for perpendicular recording is imaged in the SUL and this results in an increase in the strength of the magnetic field by approximately a factor of two. In addition, due to imaging effects, the effective number of turns on the write head is doubled for perpendicular recording. It is important for perpendicular recording that the magnetization of the magnetic material for the SUL be larger than that for the pole of the write head [51.48]. This is the case to prevent the SUL from saturating before the pole tip saturates, resulting in a decrease in the gradient of the head field, which would result in an

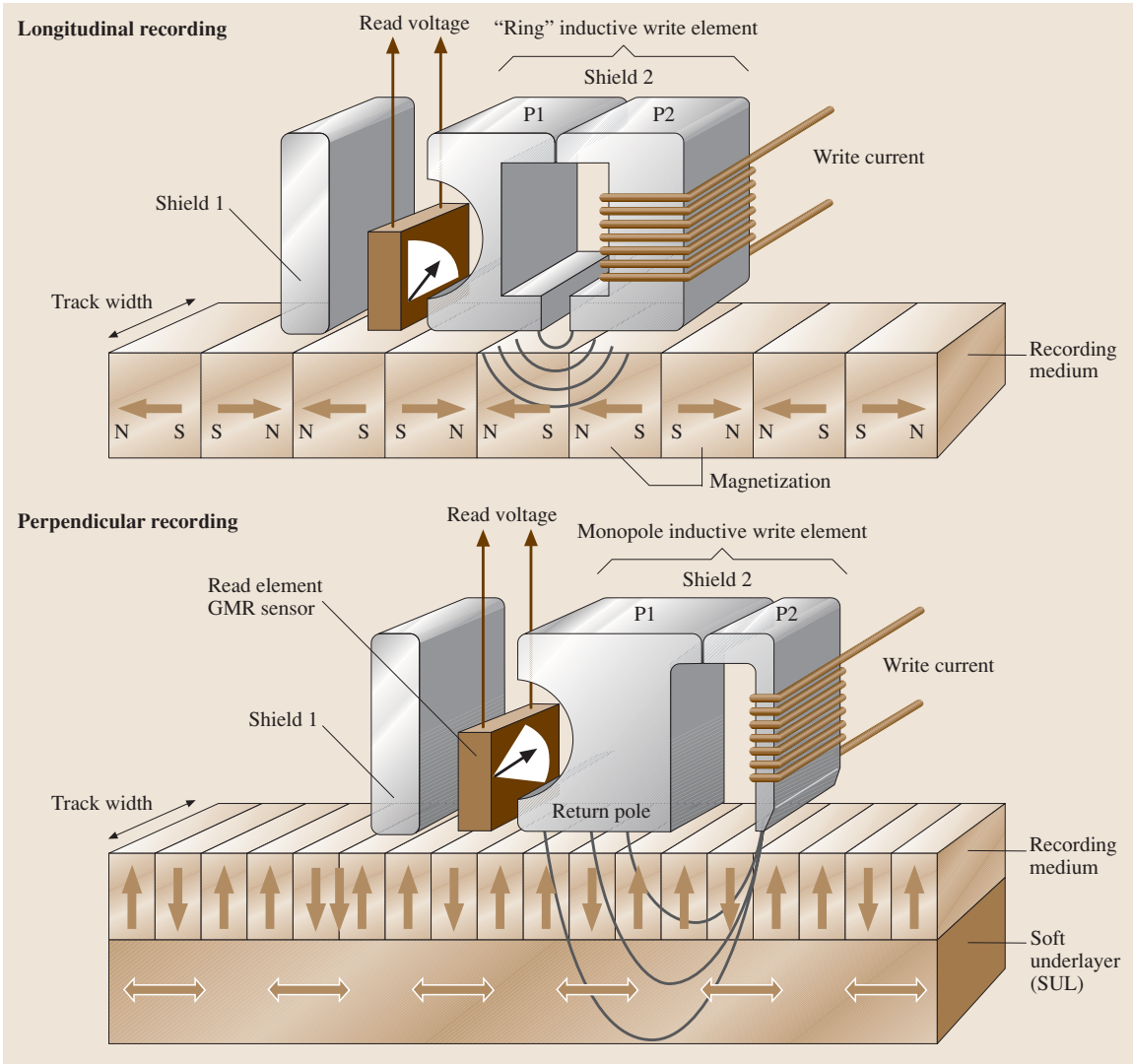

Fig. 51.27 Schematic of longitudinal and perpendicular recording systems. (After [51.1])

increased transition length (to be discussed). A large magnetic field and gradient of magnetic field from the write head can record media with a larger coercive field than for longitudinal recording, which results in a reduced transition length. Perpendicular-recording media can be made thicker than for longitudinal media for the same areal density. The media thermal stability factor $\left(\frac{K_u V}{k_B T}\right)$ is increased both by an increase in K_u by virtue of the increased coercive field but also by the increase in the volume (V) with the thicker media. Reading of the magnetic transitions with perpendicular recording is done with a spin valve head as with longitudinal recording – the difference being that with perpendicular recording the response is a step instead of a pulse (to be discussed).

A significant recent development for perpendicular write heads is the addition of a trailing-edge shield to the head that results in an improvement in the concentration of the writing flux and an increase in the gradient of the head field ($\mathrm{d}H_y/\mathrm{d}x$), which reduces the transition length [51.49,50]. A schematic of a write head with a trailing-edge shield is shown in Fig. 51.28 [51.51]. The shield connects to the larger return structure for the head shown in Fig. 51.27. The particular geometry

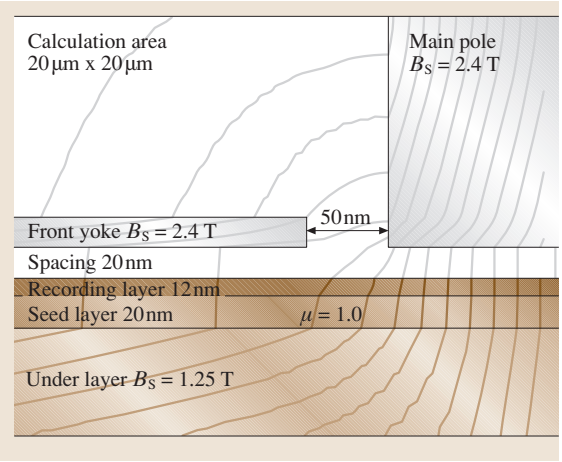

Fig. 51.28 Schematic of a perpendicular recording head including the main pole and the front yoke or trailing-edge shield. (After [51.51])

and saturation magnetization of the main pole and the *front yoke* or trailing-edge shield were used in a two-dimensional finite element model to calculate the head fields and shape of the recorded transition [51.51]. Results of the simulation of transition shape are shown in Fig. 51.29, where it is seen that the recorded transition is considerably sharper with the head with the front yoke compared with the head without the shield, particularly with the higher coercivity media ($H_c = 8000$ Oe). The perpendicular magnetic field has the amplitude reduced to one-half at a distance of $0.8d$ with the shield and $1.3d$ without the shield (assuming that the spacing of the shield is spaced by a distance d from the main pole) [51.50]. The shield shunts some of the write flux, reducing the amplitude of the write field, so it is important to keep the height of the shield short. Another advantage of the trailing-edge shield is that a horizontal component of the field is added. This field reduces the field for switching since, if the angle of the field is θ, the switching field is

$$H_{\text{switch}} = \frac{\mathrm{H}_k}{\left[(\cos\theta)^{2/3} + (\sin\theta)^{2/3}\right]^{3/2}} ,$$

where H_k is the anisotropy field of the perpendicular medium. The denominator of this equation is always larger than one and hence the switching field is reduced for angles θ larger than zero degrees.Note that this equation is the switching asteroid equation used to explain the operation of the MRAM (to be discussed).

A significant advantage of perpendicular as compared with longitudinal recording is the narrower off-track read profile as shown in Fig. 51.30 [51.50]. This improvement in read profile leads directly to increased track density. There are limitations to the achievable track density in disk drives where there is significant skew of the head with respect to the track center line. Head skew results from the fact that present disk drives

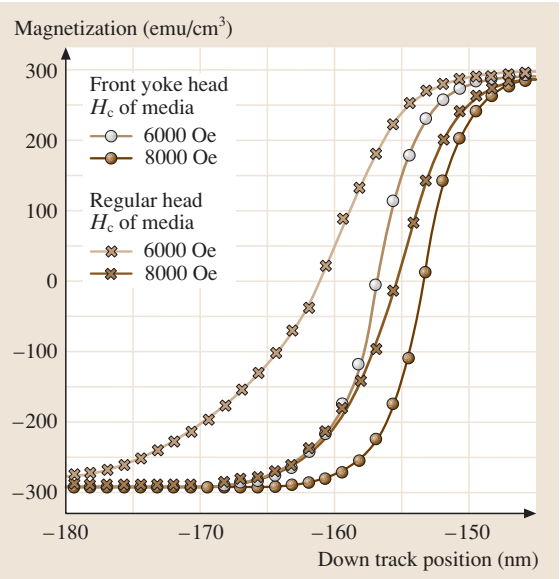

Fig. 51.29 Magnetic transitions in perpendicular recording with and without the front yoke or trailing-edge shield. (After [51.51])

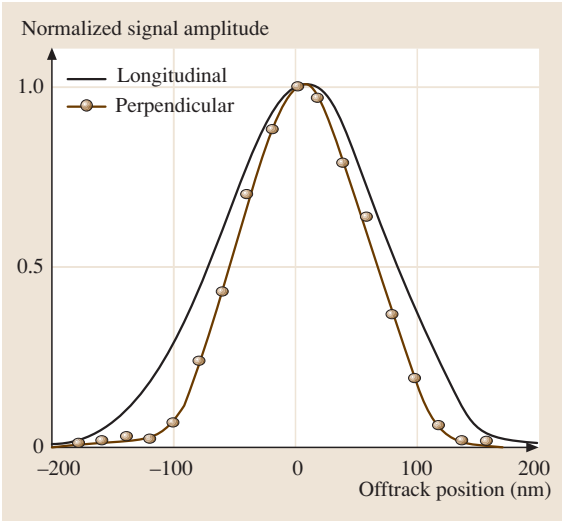

Fig. 51.30 Cross-track profile of the signal with perpendicular and longitudinal recording. (After [51.50])

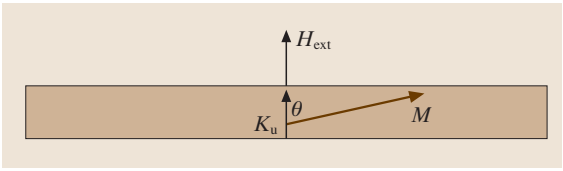

Fig. 51.31 Magnetization and perpendicular anisotropy for a perpendicular recording media. (After [51.4])

use rotary actuators and the angle of the written transition with respect to the track center line varies as the actuator is rotated across the disk, being largest at the inside and outside diameters. With head skew it is possible for the write element of the head to be placed over the guard band or adjacent track of a selected track, resulting in unwanted recording in these areas. This problem is reduced by using trapezoidal poles [51.52]. Shields can be added to the side of the head to reduce this erasure of adjacent track information; however, the processing of such shields is complex.

Media for Perpendicular Recording

The magnetization and anisotropy in a perpendicular recording film is shown as Fig. 51.31. The energy of the magnetization in the presence of the demagnetizing, anisotropy and magnetostatic energies (cgs units) is

$$E = \frac{1}{2}4\pi M_s^2 \cos^2\theta + K_u \sin^2\theta - H_{ext} M_s \cos\theta \,, \tag{51.19}$$

where the demagnetizing factor for a thin film magnetized normal to the surface is 4π. The equilibrium angle is given by the solution to

$$\frac{dE}{d\theta} = \frac{4\pi}{2}\left(-2\cos\theta\sin\theta\right) M_s^2 + 2K_u \sin\theta\cos\theta + H_{ext} M_s \sin\theta = 0 \,. \tag{51.20}$$

For stability

$$\frac{d^2E}{d\theta^2} = -4\pi\left(\cos^2\theta - \sin^2\theta\right) M_s^2 + 2K_u\left(\cos^2\theta - \sin^2\theta\right) + H_{ext} M_s \cos\theta > 0 \,. \tag{51.21}$$

The solution is $\sin\theta = 0$ ($\theta = 0°$ or $180°$) and the stability condition for $H_{ext} = 0$ results in

$$K_u > 2\pi M_s^2 \,. \tag{51.22}$$

Alloys under consideration for perpendicular recording include those listed in Table 51.6 [51.53] and Table 51.7. A review of work on perpendicular recording media was published [51.54]. It is observed from this table that these candidate materials satisfy the condition (51.22). The critical magnetic field below which the $\theta = 0°$ solution is no longer stable is given by the solution to (51.21) with $H_{ext} \neq 0$, resulting in

$$H_{e,crit}(\theta = 0°) = -\frac{\left(2K_u - 4\pi M_s^2\right)}{M_s} \,,$$
$$H_{e,crit}(\theta = 180°) = \frac{\left(2K_u - 4\pi M_s^2\right)}{M_s} \,. \tag{51.23}$$

The solution to (51.21) with $\sin\theta$ factored out is

$$-4\pi M_s^2 \cos\theta + 2K_u \cos\theta + H_{ext} M_s = 0 \,,$$
$$H_{ext} = \cos\theta\left(4\pi M_s - 2K_u/M_s\right) \,,$$
$$M_\perp/M_s = \cos\theta \,,$$
$$M_\perp/M_s = \frac{H_{ext}}{\left(4\pi M_s - 2K_u/M_s\right)} \,. \tag{51.24}$$

This solution applies when the magnetization curve is not saturated. $H_{e,crit}$ is not the same as the coercive field where $M(H_{ext}) = 0$. The coercive field is found from (51.20) by recognizing that the magnetic field $H_{ext} = -|H_{e,crit}| - H'$, where H' is measured from $-|H_{e,crit}|$. The coercive field is then

$$H_c = -2\left|H_{e,crit}\right| \,.$$

The result for a Co–Cr–Pt alloy (Table 51.7) with the following parameters: $K_u = 1.45\times10^6$ erg/cm^3, $M_s = 280$ emu/cm^3 is as follows

$$H_{e,crit}(\theta = 0°) = -\frac{\left(2K_u - 4\pi M_s^2\right)}{M_s} \,,$$
$$H_{e,crit}(\theta = 0°) = -\frac{\left(2\times1.45\times10^6 - 4\pi 280^2\right)}{280} \,,$$
$$H_{e,crit}(\theta = 0°) = -6838\,\text{Oe} \,,$$
$$H_{e,crit}(\theta = 180°) = 6838\,\text{Oe} \,.$$

Table 51.6 Magnetic properties of selected materials for perpendicular recording (data from [51.53])

Material	H_k (kOe)	M_s (emu/cm^3)	K_u (erg/cm^3×10^6)	$2\pi M_s^2$ (emu/cm^3)^2
Co–Cr	7	270	0.95	0.46
Co–Cr–Pt	10	280	1.45	0.49
Co/Pd	17	350	2.98	0.77
Fe/Pt	28	750	10.5	3.53

Table 51.7 Media for perpendicular recording

Media	H_c (kOe)	M_r (emu/cm^3)	α ($4\pi M_r/H_c$)	H_k (kOe)	Magnetic layer thickness (nm)	H_n (kOe)	Comments	Ref.
CoCrNbPt/Ti	2–5	250–450	1.25	6	50	–	Good SNR, poor thermal stability	[51.55]
CoCrPt/Ti/CoZr	2–4	500	2.09	13	25	–	Good SNR, poor thermal stability	[51.56]
$Co_{70.3}Cr_{15}Pt_{14.7}$/Ti/CoZrNb	5.5	460	1.05	–	–	−1.7	Good thermal stability, SNR = 25 dB	[51.57]
$[Co/Pd]_n$	2–10	200–600	0.84	15–30	10–50	–	Good thermal stability, poor SNR	[51.58]
$[Co/PdSi]_{13}$	3.2–5.4	160	1.35	–	–	–	SNR improved	[51.59]
FePt	2–5	800	2.87	> 30	10–50	–	–	[51.60]
CoCrPtB/Ti–CoCrTa/laminated SUL	2.5–3.0	400	1.83	12	–	–	Good SNR, poor thermal stability	[51.61]
CoCrPtO/Ti–Ru/laminated SUL	3.5	520	1.86	–	–	–	Good thermal stability, poor SNR	[51.62]
CoPtCr–SiO_2	> 5	430	1.08	18.6	10–30	–	Good thermal stability, good SNR	[51.63]
Coupled/granular/continuous CoCrPt/Co–Pt	4–5	400	1.11	–	–	−1 to −3	Good thermal stability, good SNR	[51.64]
Coupled/granular/continuous $CoCr_{18}Pt_{12}$/Co–Pt	4.02	395	1.23	–	–	−1.8	Good thermal stability. SNR = 31 dB	[51.65] [51.66] [51.67]

The magnetization curve for the second quadrant is:

$$M_\perp/M_s = \frac{H_{ext}}{(4\pi M_s - 2K_u/M_s)} ,$$

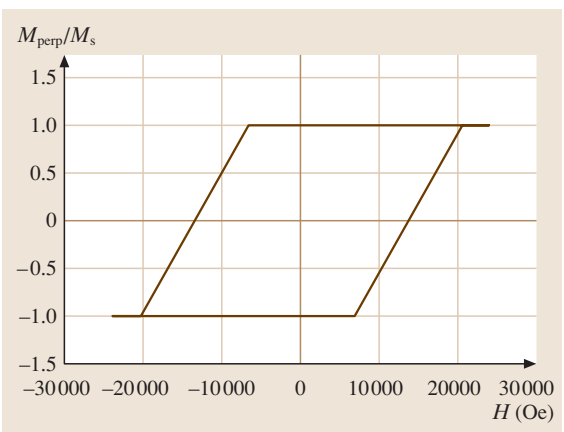

Fig. 51.32 Hysteresis curve for Co–Cr–Pt perpendicular recording media using the analysis in the text

$$M_\perp/M_s = \frac{(H_{ext} + 2\times|H_{e,crit}|)}{|H_{e,crit}|} ,$$

$$H_c = -2\times|H_{e,crit}| = -13.67\,\text{kOe} .$$

The magnetization curve for the fourth quadrant is:

$$M_\perp/M_s = \frac{(H_{ext} - |H_{e,crit}|)}{|H_{e,crit}|} - 1 .$$

The magnetization curve is shown in Fig. 51.32 and exhibits the desired large coercivity but the curve is sheared due to the large demagnetizing field.

In general, the magnetic hysteresis curve (M versus H_{ext}) for the recording medium is as illustrated in Fig. 51.33 [51.53]. Here the slope parameter (α) characterizes the slope of the magnetization curve at $H = -H_c$,

$$\alpha = 4\pi\left(\frac{dM}{dH}\right)_{H=-H_c} . \qquad (51.25)$$

Finite values of α result from variations in the direction of the perpendicular magnetization, dispersion in the

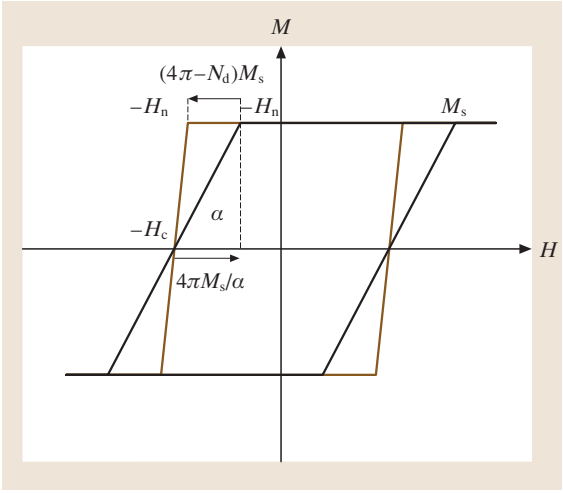

Fig. 51.33 Hysteresis curve with demagnetizing field $(4\pi M_s/\alpha)$ and a reduced demagnetizing factor N_d for a perpendicular recording film with loop slope parameter α. (After [51.53])

perpendicular anisotropy and variations in the exchange coupling between grains and clusters in the media. The effective demagnetizing field is reduced from $4\pi M$ to $4\pi M/\alpha$. This reduction in demagnetizing field results from the formation of a rectangular checkerboard pattern of domains with high-density linear recording and high track densities [51.53]. The effective anisotropy energy, which assists in overcoming the thermal energy and the superparamagnetic limit, is given in terms of the nucleation field (H_n'), at which field the magnetization just starts to reverse, by

$$K_{eff} = H_n' M_s/2 \,.$$

For high areal density an estimate of the reduced demagnetizing factor is

$$N_d' = 0.5 \times 4\pi M_s$$

and the increase in the nucleation field H_n is

$$H_n' = H_n + \frac{4\pi M_s}{2} \,.$$

For high-density recording large values for α and H_c are required; however, the value of H_c is limited by the ability of the pole head to generate magnetic fields equal to or greater than approximately $1.5 \times H_c$, the condition that ensures adequate overwrite.

The transition parameter (a) for perpendicular recording can be estimated using the same write-slope

Table 51.8 Parameters for evaluating transition parameters for longitudinal and perpendicular recording

Parameter	a_L	a_P
d (nm)	26	26
t (nm)	–	50
u (nm)	–	0
S^*	0.95	0.98
M_r (emu/cm^3)	200	200
δ (nm)	14	–
Q	0.6	0.6
$H_{c,max}$ (Oe)	3500	8000

criteria discussed for longitudinal recording [51.68]. Here,

$$\frac{dM}{dx} = \frac{dM}{dH}\left(\frac{dH_{head}}{dx} + \frac{dH_{demagnetizing}}{dx}\right) \,. \quad (51.26)$$

This equation is solved by assuming an arctangent transition shape and denoting the slope of the head field by $\frac{dH_{head}}{dx} = QH_c/s$, where s is the total spacing of the write pole tip to the top of the SUL, consisting of the physical spacing (d), the thickness of the recording media (δ) and the spacing between the SUL and the magnetic recording film (u). Using the demagnetizing field for a perpendicular transition [51.69]

$$a = a_1 + \sqrt{\left(a_1^2 + \frac{(1-S^*)\,\delta s}{\pi Q}\right)} \,,$$

$$a_1 = \frac{4M_r s}{QH_c} + \frac{s\,(1-S^*)}{\pi Q} - \frac{\delta}{4} \,, \quad \alpha = \frac{\frac{4\pi M_r}{H_c}}{(1-S^*)} \,. \quad (51.27)$$

A comparison between the transition parameters for longitudinal (a_L) and perpendicular (a_P) recording from (51.5) and (51.27) with the parameters listed in Table 51.8 is shown in Fig. 51.34 [(H_c) for longitudinal recording is the dark line and (H_c) for perpendicular recording is dashed]. It is seen that the transition parameter for perpendicular recording can be made smaller than that for longitudinal recording if the coercive field for perpendicular recording is larger than 6500 Oe. Note that the thickness of the recording media for perpendicular recording is larger than that for longitudinal recording. The magnetic squareness (M_r/M_s) for perpendicular recording media is larger than that for longitudinal recording.

Gao and *Bertram* have shown a significant advantage for perpendicular recording if the uniaxial anisotropy is not aligned perpendicular to the surface, but oriented at

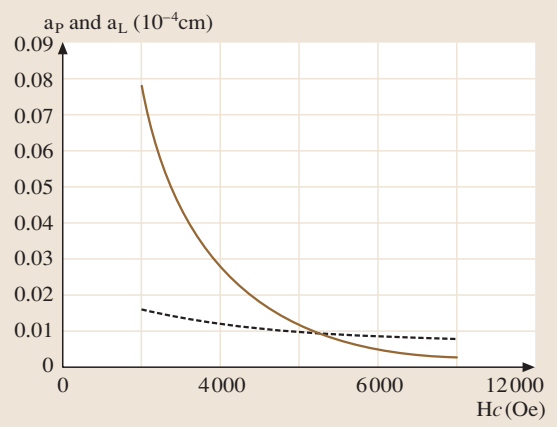

Fig. 51.34 Comparison of transition parameters versus the coercive field (H_c) for perpendicular (*solid line*) and longitudinal (*dashed line*) recording. (After [51.68])

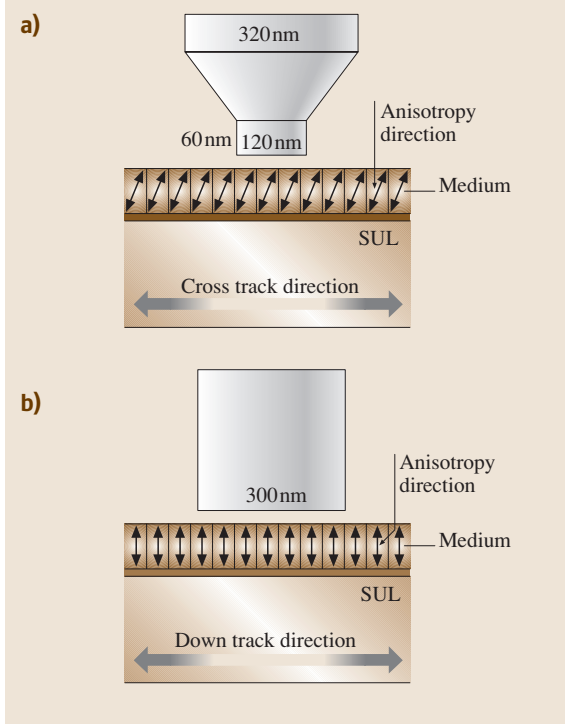

Fig. 51.35 Typical geometry of tilted perpendicular recording. The medium anisotropy directions and not the medium grains are tilted in the cross-track direction. (After [51.70])

45° to the perpendicular [51.70]. The geometry for this *tilted* perpendicular recording is shown as Fig. 51.35. The crystallites comprising the media are still aligned perpendicular but the crystalline anisotropy is assumed to be at 45°. No material system was disclosed that exhibits this tilted anisotropy. With tilted perpendicular recording the crystalline anisotropy field (H_k) can be made significantly larger than if the anisotropy is perpendicular. An example is 15 000 Oe for perpendicular recording and 28 000 Oe for tilted perpendicular recording [51.70]. Some of the advantages of tilted perpendicular recording are: reduced switching field and reduced average grain diameter, resulting in increased signal-to-noise ratio since the number of grains per bit is increased.

The requirements for media for ultra-high-density perpendicular recording have been analyzed [51.71]. Table 51.9 summarizes the results for media parameters for areal densities of 100–1000 Gb/in^2. Several key media parameters are the grains per bit (N) and the coercivity (H_c). An estimate of the signal-to-noise (SNR) ratio using the Poisson statistics of additive noise for the magnetic grains is

$$\mathrm{SNR} = -10 \log_{10}(N) \ ,$$

where N is the number of magnetic grains per bit [51.71]. There are two approaches to realizing recording media with a large perpendicular anisotropy and that can approach the parameters in Table 51.9: granular media typified by CoCr alloys and *continuous* multilayer media typified by $[\mathrm{Co–Pd}]_n$ multilayers. CoCr alloys exhibit good SNR but insufficient H_c for ultra-high recording densities, while the multilayers have not exhibited sufficient SNR. Recent results for multilayers of Co/PdSi where the Pd layer is doped with silicon have shown an improvement in the SNR [51.59]. The technology demonstration of $50+$ Gb/in^2 (to be discussed) used a granular CoCr alloy. Table 51.7 is a listing of some metal alloy candidates for perpendicular recording. In general, Pt plays a significant role in determining the magnetic anisotropy and Cr, Ta, Nb and B reduce the exchange coupling, resulting in reduced noise. Another alternative for perpendicular recording media is oxide media, e.g., CoCrPtO or $\mathrm{CoCrPt–SiO_2}$ [51.63, 72, 73]. A recent study has shown that the oxide media has improved coercivity and a negative nucleation field (H_n), reduced pulse width and reduced signal decay compared to CoCrPtB media [51.74]. An issue with the oxide media is the nonuniformity of the coercivity and oxygen content in the disk surface due to the high gas pressure and oxygen-gas reactive sputtering [51.74]. The last two listings are for a *coupled granular/continuous* (CGC) medium that combines the best properties of the continuous media (high H_c and good thermal stability) and gran-

Table 51.9 Requirements for perpendicular recording media for ultrahigh recording densities (after [51.71])

Areal density (Gb/in^2)	100	250	500	1000
Flying height d (nm)	8	7	6	5
Signal-to-noise ratio (RMS signal/RMS noise)	18	17	16	15
Grains per bit N	63	50	40	32
Average grain diameter D (nm)	9	7	5	4
S^*	1	1	1	1
Media thickness δ (nm)	18	20	22	24
Perpendicular anisotropy constant K_u($\times 10^6$ erg/cm^3)	2	3	4	6
Saturation magnetization M_s (emu/cm^3)	400	550	700	875
Coercivity H_c (Oe)	8500	11000	12500	14300

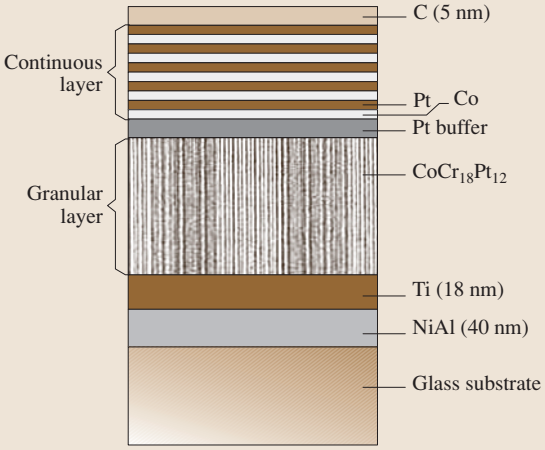

Fig. 51.36 Schematic representation for coupled granular/continuous (CGC) media. (After [51.64])

ular media (good SNR) [51.64, 65, 75]. A cross section of the CGC media is shown in Fig. 51.36 [51.64]. The continuous layer causes an exchange coupling which stabilizes the granular medium; this exchange field is large ($\approx$ 200 kOe) and can result in considerable improvement in thermal stability [51.75]. The initial results for CGC media were encouraging from the standpoint of thermal stability but the high-density SNR was 2 dB less than for the granular media alone. Further optimization of the CGC media using $[Co–Pt]_n$ multilayers coupled through a Pt buffer layer to a CoCrPt granular layer has shown an improvement in SNR over the granular media alone by 3–5 dB [51.75]. The improvement in SNR is believed to be due to the fact that magnetic recording transitions in the continuous layer are in the form of narrow domain walls and the magnetic interaction between the two layers may result in breaking up the magnetic clusters that form the transitions in the granular medium [51.75].

Magnetic materials used for the soft underlayer (SUL) for a perpendicular recording media must be magnetically soft for low reluctance but also must not exhibit magnetic domains, which can contribute noise to the read signal. The SUL must have a magnetic moment that is larger than that for the pole tip of the write element so that the SUL saturates *after* the pole tip saturates. This condition assures that there is no excess reluctance directly under the pole tip. The SUL must also be thick enough that the reluctance of the path through which the flux travels allows the maximum magnetic field under the gap. Decreasing the reluctance of the flux path also increases the gradient of the magnetic field from the pole, which reduces the length of the transition parameter (51.20) [51.48]. A guide for selecting the SUL thickness (T_{SUL}) is

$$T_{SUL} \approx \frac{A_{\text{pole tip}}}{C_{\text{pole tip}}} \frac{M_{\text{pole tip}}}{M_{SUL}} , \qquad (51.28)$$

where $A_{\text{pole tip}}$ and $C_{\text{pole tip}}$ are the area and the circumference of the pole tip, respectively, and $M_{\text{pole tip}}$ and M_{SUL} are the saturation magnetizations of the pole tip of the write head and soft underlayer, respectively [51.48]. The effects of changing the thickness of the SUL on the recording parameters of a probe head are shown in Table 51.10 [51.48], where it is seen that the thickness and hence reluctance are key to head performance. Candidate materials for the SUL are listed

Table 51.10 Effect of the thickness of the FeAlN soft underlayer (SUL) on recording head parameters (after [51.48])

Thickness of FeAlN SUL ($4\pi M_s = 20$ kG)	0.1 μm	0.3 μm
Maximum magnetic field (kOe) at recording layer at saturation current (mA) (in parentheses)	16.3 (90)	17.7 (70)
Maximum head field gradient (Oe/nm)	175	550

Table 51.11 Magnetic materials for soft underlayers (SUL)

Material	B_s (kG) ($T\times10^{-1}$)	Relative Permeability	Comments	Reference
$Ni_{80}Fe_{20}$ (Permalloy)	10	1500–2000	Insufficient magnetic moment for SUL. Field gradient decreases at maximum field	[51.48]
Sendust (FeSiAl)	10	8000	Insufficient magnetic moment for SUL	[51.4]
FeAlN	20	2000	Sensitive to process conditions; believed to be less useful than FeCoB	[51.48]
FeCoB	20–24	200–240	Annealed to reduce stress	[51.76,77]
CoZrNb	14		Lower magnetostriction than FeCoB	[51.77]
$NiFe_{17}Mo_4$				[51.78]
$[Ni–Fe/Si]_n$			Multilayers	[51.79]
IrMn/CoZrNb	14		IrMn antiferromagnetic film to reduce spike noise due to domain walls	[51.80]

Table 51.12 Parameters for perpendicular recording demonstrations

Demonstration	52.5 Gb/in^2	≈ 100 Gb/in^2
media		
Type	CoCrPt	CoCrPt
M_s (emu/cm^3)	250	330
H_c (kOe)	2.6	4.94
K_u (erg/cm^3)	$H_k = 10$ kOe	1.82×10^6
S	0.98	0.92
$\langle D\rangle$ (nm)	–	11.9
Underlayer	FeTaC (16 kG) 400 nm	–
Head		
Turns	–	1
Fly height (nm)		6.4
Magnetic spacing (nm)	20	–
Pole material	FeNi (16 kG)	–
Pole width (nm)	250	105
Pole thickness (nm)	400	105
Write width (nm)	≈ 250	180
Shield–shield spacing (nm)	80	70
Read width (nm)	200	100
Component performance		
Sensitivity (mV/μm)	3	25
PW_{50}		70
Channel performance		
Channel type	Simulator (code rate = 32/33)	Software (code rate = 16/17)
Bit density (kb/in)	590	650
Track density (ktr/in)	88.9	143
Areal density (user/channel) (Gb/in^2)	52.5 (user)	84 (user) 93 (channel)
On-track bit error rate	10^{-5}	6.7×10^{-5}

in Table 51.11. A major issue with the soft underlayer is the motion of domain walls driven by the magnetic field from the write head which can lead to *spike* noise. The last entry in Table 51.11 is for an antiferromagnetic pinning layer to prevent the motion of such domain walls.

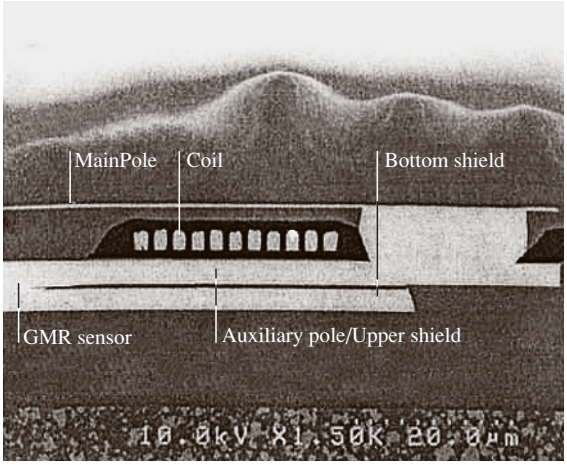

Fig. 51.37 Cross-sectional view of a perpendicular head with a GMR sensor including the bottom and upper shields. The upper shield also serves as the auxiliary pole. (After [51.81])

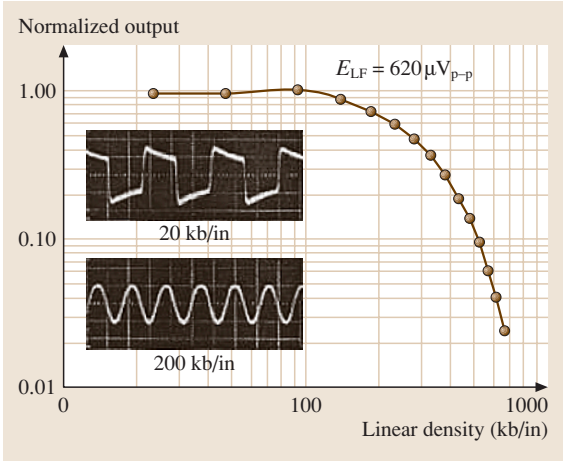

Fig. 51.38 Normalized voltage amplitude for a sequence of read signals from a perpendicular recording system versus linear density in kb/in. (After [51.81])

Perpendicular Recording Demonstrations

Perpendicular recording has now been used in commercial disk drives. The first was the Toshiba 40 GB, 1.8 inch disk drive with an areal density of approximately 75 Gb/in^2, while more recently the capacity has been increased to 80 GB and the areal density to 133 Gb/in^2 (Toshiba 2006). Seagate has shipped 2.5 inch notebook drives with a capacity of up to 160 GB and an areal density of 132 Gb/in^2 (Seagate 2006).An earlier technology demonstration with an areal density of 52.5 Gb/in^2 was reported in 2001 [51.81] and one for approximately 100 Gb/in^2 in 2003 [51.82]. Recently, Hitachi Global Storage Technologies has reported an areal density of 230 Gb/in^2 using perpendicular magnetic recording and a tunneling current-perpendicular-to-the-plane (CPP) GMR read head (to be discussed) [51.83]. We show in Table 51.12 the parameters used for the two areal density demonstrations. In both cases a pole write head and a spin valve read head were used. The parameters for the ≈ 100 Gb/in^2 demonstration are close to those required for the ultra-high densities (> 100 Gb/in^2) as described in Table 51.9, except that the coercivity is about one half that specified. A cross section of the write and read elements for the perpendicular recording head used in the 52.5-Gb/in^2 demonstration is shown in Fig. 51.37 [51.81]. The pole of the write head is identified as the "main pole" and the thick return pole and upper shield of the GMR sensor are identified as the "auxiliary pole/upper shield". The read signal versus density (roll-off curve) for the 52.5-Gb/in^2 demonstration is shown in Fig. 51.38 and results from the increasing interference of positive and negative step pulses in a long string of transitions. At low densities a step response is observed in perpendicular recording since the GMR sensor detects the vertical component of the stray magnetization that reverses at the transition and at higher densities the response appears as a sinusoid. The decay in the signal at the low-density response is due to the insufficient bandwidth of the preamplifier. The read signal for isolated transitions can be described by the response function

$$h(t) = A \tanh\left(\frac{\ln 3}{T_{50}} t\right) , \qquad (51.29)$$

where A is one half of the signal amplitude and T_{50} is the time for the signal to rise from $-A/2$ to $A/2$. The step signals can be detected either by differentiating the signal to produce pulses, as with longitudinal recording, or with equalizer circuits that directly handle the step response. The channel performance as realized with simulator channels is listed in Table 51.12 and approximates the requirements of a practical system.

Seagate technology reported an areal density of 100 Gb/in^2 in November 2002 [51.84]. The linear density was 700 kb/in and the track density was 143 ktracks/in. Seagate has also reported an areal density of 170 Gb/in^2. The linear density was 1050 kb/in and the track density was 161 ktracks/in with a data rate of 483 Mb/s. However, in neither case was this areal density reported in a disk-drive product but rather was measured using a single disk and single head [51.85].

51.2 Magnetic Random-Access Memory

The application of the giant-magnetoresistive effect to recording heads that we have discussed assumed that the sense current is in the plane of the recording film. This is not the only possibility and devices with the current perpendicular to the plane (CPP) have been proposed both for magnetic recording read heads but also for fast magnetic random-access memory (MRAM). The CPP technology that shows the most promise for both the magnetic recording and memory application is the magnetic tunnel junction (MTJ). The MTJ involves a pinned and a free ferromagnetic film spaced by a thin *insulating* film, usually Al_2O_3. Figure 51.39 shows the schematic of an MTJ used for the MRAM application, including orthogonal bit and word or digit lines and the stack of films comprising a basic MTJ [51.86, 87]. Figure 51.40 shows a more detailed stack of films for an MTJ, including synthetic antiferromagnetic films, antiferromagnetic pinning films and the free film. A typical MTJ has the following thickness values for the key films: antiferromagnet: 300 Å, $Co_{90}Fe_{10}$ ferromagnet: 20 Å, ruthenium: 8 Å, Al_2O_3: 10–15 Å, $Co_{90}Fe_{10}$ ferromagnet: 20 Å. As for the spin valve, the use of $Co_{90}Fe_{10}$ films for the free layer enhances $\Delta R/R$ [51.20]. Figure 51.40 also shows $\Delta R/R$ for a typical MTJ (for a bit area of $0.6\times1.2\,\mu m$) versus magnetic field with the multiple curves being taken over a 6-inch wafer: the maximum change is greater than 48% [51.87]. The change in resistance with orientation of the free layer relative to the pinned layer is significantly larger than for GMR technology, but a thin insulating layer between the ferromagnetic films is required. The memory architecture that has evolved has a single MOS transistor coupled to the MTJ and the word line. The current in the word line supplies the magnetic field along the easy axis of the free film and is insulated from the MTJ (Fig. 51.39). Switching of a soft-magnetic film with a magnetic field applied along the direction of an induced uniaxial anisotropy (the easy axis) and simultaneously along a direction orthogonal to the easy axis (the hard axis) has been discussed (e.g., [51.4]). The switching is described by a switching asteroid given by the following equation and shown in Fig. 51.41 (in the figure the easy and hard magnetic fields are normalized with respect to the anisotropy field H_k).

$$(H_{\text{easy}})^{2/3}+(H_{\text{hard}})^{2/3}=(H_k)^{2/3}$$

$$H_k=2\frac{K_u}{M}$$

Switching of the state of the magnetization will occur whenever the combination of easy- and hard-axis fields is on the outside of the asteroid. The switching field can be significantly reduced if magnetic fields are applied along both the easy- and hard-axis directions and an optimum is to have the fields equal. The bit line is used to supply the hard-axis magnetic field and the word line the easy-axis field. For writing a bit the sense transistor is turned off and current pulses are applied along both orthogonal conductors, generating a magnetic field at the free film sufficient in amplitude to switch the magnetization of the free film. For reading a bit, the sense transistor is turned on by the word line and pulses of current are driven along the bit line (with the amplitude of the magnetic field insufficient to switch the free film) and the current is either high when the ΔR is low, corresponding to say a 1 or the current amplitude is low when ΔR is high, corresponding to a 0. Without the sense transistor there would be many *sneak paths* for the current through other MTJs, reducing the available current for reading the selected bit. The MTJ memory technology shows considerable promise for replacing semiconductor SRAM and DRAM memories, primarily because of the nonvolatility of the memory in the MRAM technology. The speed for reading data is comparable to that of SRAM and the density is comparable to that for DRAM.

The physics of the MTJ is different from that for GMR [51.88]. Ferromagnetic films have two types of

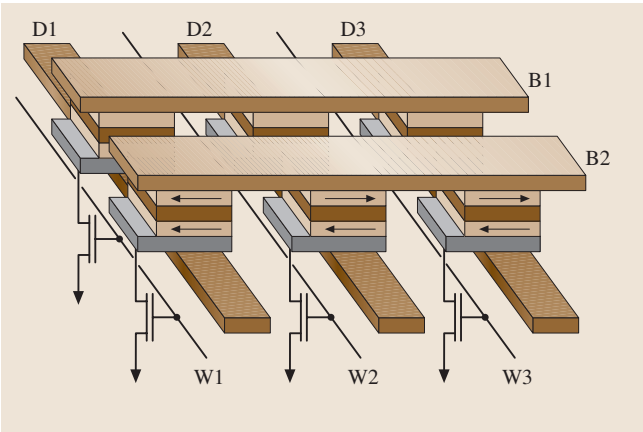

Fig. 51.39 Schematic of MRAM cross-point architecture with bits between orthogonal conductors and each cell defined by one MTJ and one transistor. The top lines in contact with the top electrode of the bits provides hard-axis fields, while the bottom lines are isolated and provide easy-axis fields. Turning on the transistor provides a current path so that the corresponding bit can be sensed. (After [51.86])

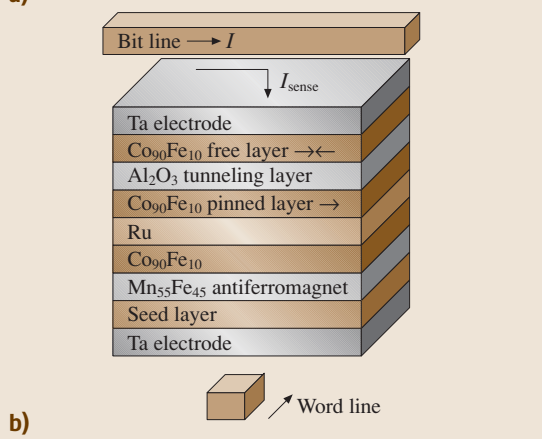

Fig. 51.40 **(a)** Stack of films comprising a typical MTJ. The arrows show the direction of the magnetizations in the two coupled films. **(b)** Hysteresis curves of $\Delta R/R$ versus magnetic field for $0.6\times1.2\,\mu$m bits on a 6-in wafer. (After [51.87])

electrons: those polarized parallel to the magnetization (↑) and those polarized antiparallel to the magnetization (↓). A polarization ratio (P) for a ferromagnetic material can be defined as

$$P = \frac{D(E_F)^{\uparrow} - D(E_F)^{\downarrow}}{D(E_F)^{\uparrow} + D(E_F)^{\downarrow}} ,$$

where $D(E_F)^{\uparrow}$ and $D(E_F)^{\downarrow}$ are the densities of states for electrons at the Fermi energy for the spin-up and spin-down electrons, respectively. The magnetoresistance ratio of two films coupled by an insulator is [51.89]

$$\frac{\Delta R}{R} = \frac{R_a - R_p}{R_p} = \frac{2P_1P_2}{1 - P_1P_2} , \qquad (51.30)$$

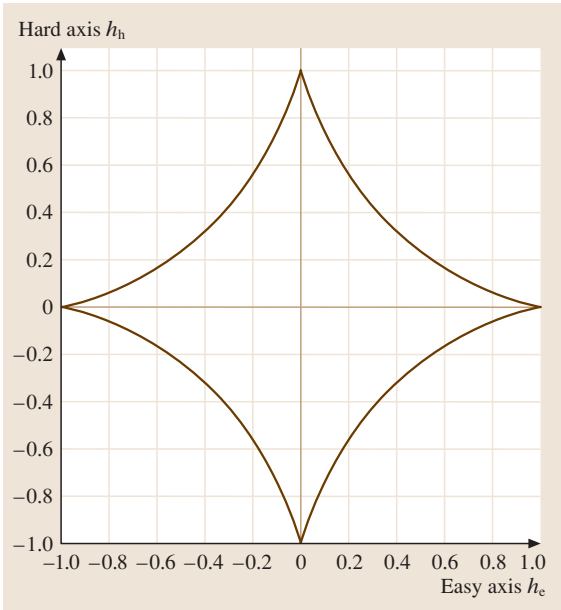

Fig. 51.41 Switching asteroid plotted with magnetic fields normalized to the induced anisotropy field ($2K_u/M$). The ferromagnetic film will switch for any combination of easy- and hard-axis fields on the outside of the asteroid

where R_a and R_p are the resistances of the coupled films in the antiparallel and parallel configurations, respectively, and the spin polarizations are P_1 and P_2 for the two ferromagnetic films. Values of the spin polarization ratio are: $P_{Co} \approx 0.35$, $P_{Fe} \approx 0.44$ and $P_{Permalloy} \approx 0.3$ [51.88]. With cobalt used as one electrode and Permalloy for the other electrode, the predicted value for $\Delta R/R$ is 24%. Conduction through the insulating film is by quantum-mechanical tunneling, described by a transmission coefficient (T)

$$T = \frac{|\psi_{transmitted}(x)|^2}{|\psi_{incident}(x)|^2} ,$$

where $\psi(x)$ is the wavefunction for the electron plane wave and $|\psi(x)|^2$ is the probability of finding an electron at the position x. The transmission coefficient is a measure of the resistance of the barrier. The transmission coefficient for electrons with energy E tunneling through an insulating film of thickness a with amplitude of the barrier height of V_0 is given by

$$T = T_0\, e^{-2\alpha a} ,$$

where

$$T_0 = \frac{16E\,(V_0 - E)}{V_0^2} ,$$

Table 51.13 Parameters for Permalloy ($Ni_{80}Fe_{20}$)

M_s (T)	K_1 (J/m^3)	A (exchange constant) (10^{-12} J/m)	Critical length l_s (nm)
1.0	500	13	5.7

and

$$\alpha^2 = \frac{2m\,(V_0 - E)}{\hbar^2}\,.$$

This result applies when $\alpha a > 1$. A barrier height of 10 eV applies for CoO. The exponential dependence of the transmission coefficient on the thickness of the barrier shows the requirement for a thin barrier. A typical value of the thickness of an Al_2O_3 layer is 10 Å and the resistance changes by a factor of 100 million in changing the thickness from 0 to 10 Å. The reason that the MTJ is more attractive than a spin valve for the memory application is that the MTJ can be made with a resistance of many ohms, while the spin valve is nearly a short circuit. The use of the synthetic antiferromagnet for the MTJ also helps to avoid the superparamagnetic limit for this device, since the films comprising the synthetic antiferromagnet are thicker than the single antiferromagnetic film that was used to pin one of the ferromagnetic electrodes.

A significant problem with the MTJ is the different magnetic states that can be found depending on the size and shape of the bit. A review of an analysis of the states for a rectangular-shaped bit has been published [51.90] and we will quote some of their results to illustrate the problem. The analysis uses finite element analysis to solve the equation of motion for the magnetization ($\boldsymbol{M}$) with Gilbert damping in the presence of an effective magnetic field ($\boldsymbol{H}_{\text{eff}}$)

$$\frac{\mathrm{d}\boldsymbol{M}}{\mathrm{d}t} = \gamma\,(\boldsymbol{M}\times\boldsymbol{H}_{\text{eff}}) - \frac{\alpha}{M}\left(\boldsymbol{M}\times\dot{\boldsymbol{M}}\right)\,. \qquad (51.31)$$

The effective magnetic field can be derived from the magnetic free-enthalpy density

$$\boldsymbol{H}_{\text{eff}} = -\delta g/\delta \boldsymbol{M}$$

and the magnetic free enthalpy per unit volume is given by the sum of terms

$$g = g_{\text{exchange}} + g_{\text{anisotropy}} + g_{\text{demagnetizing-field}} + g_{\text{external-field}}\,.$$

An example of this analysis is a rectangular film of thickness 20 nm, length 1 μm, width 1 μm with magnetic properties shown in Table 51.13. The exchange constant is $A = s^2a^2J_{\text{ex}}N_{\text{v}}/2$, where s is the spin of the atom, a the lattice constant and N_{v} is the number of nearest-neighbor atoms per unit volume. The critical length determines the maximum size of the mesh used in the finite element analysis. Figure 51.42 shows three of the six states of the magnetization in the sample. The first two are high-remanence states referred to as S-type and C-type and can be formed if the starting conditions are a single-domain state. The last state shown is a low-remanence state with an off-center vortex. The last state is formed when the initial conditions are two domains along the long axis of the film. The total energies for the three states are shown in Table 51.14 and it is seen that the lowest energy is the low-remanence state. An issue with the MRAM is the possibility of exciting the different states in the storage cell that can then result in a different switching asteroid. Thin films with low-aspect-ratio bit shapes have been predicted to result in reduced propensity to excite the vortex structures [51.91]. Changing the shape of the bit may also assist in minimizing the vortex structures. Software for analyzing these problems is the LLG Micromagnetics Simulator™ developed by M. R. Scheinfein (llg@dancris.com).

A recent development in MRAM architecture is to pass the write current through the MTJ to heat the element and to lower the threshold for writing [51.92].

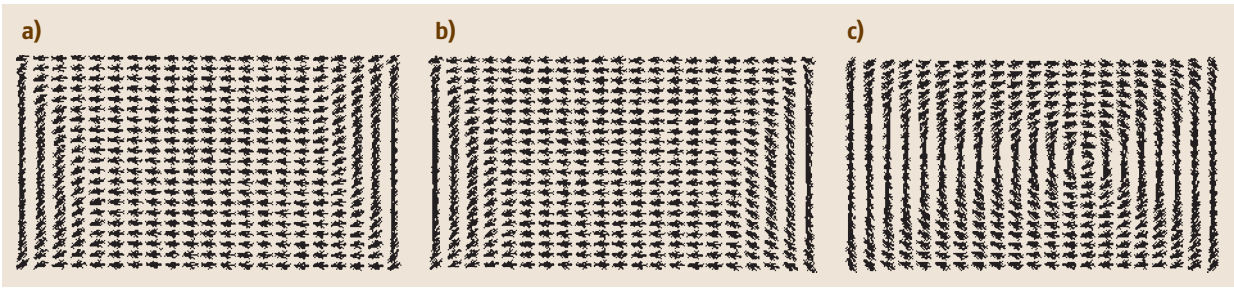

Fig. 51.42a–c Configurations for spins in a Permalloy sample described in Tables 51.13 and 51.14. Figure **(a)** is an S-state, **(b)** is a C-state and **(c)** is an off-center vortex state. (After [51.90])

Table 51.14 Total energies for different spin configurations in the Permalloy film (described in the text and Table 51.13) (after [51.90])

Structure	G (10^{-18} J)
S-state	169 897
C-state	169 890
Shifted vortex state	79 616

This is accomplished by turning on the selection transistor (Fig. 51.39) during the write operation. The advantages of this modification to the MRAM architecture are:

1. since the selection at write is controlled by the temperature, selection errors are reduced,
2. the write threshold is reduced,
3. thermal instability limits are increased by using materials with larger switching fields at the operating temperature [51.92].

51.2.1 Tunneling Magnetoresistive Heads

Tunneling magnetoresistance (TMR) can be used in a magnetic recording read-head application. These TMR heads use the CPP orientation of the sense current and, as with the MRAM, the tunneling is done through a thin insulating barrier. A schematic at the air-bearing surface in the simplest form of such a TMR head is shown as Fig. 51.43 [51.93]. The insulating barrier (again usually fabricated from Al_2O_3 films) is shown on edge and the current flow is in the plane of the paper. Longitudinal bias to put the ferromagnetic TMR electrode films in a single-domain state and the top and bottom shields are shown. The GMR ratio with the TMR effect is large but the resistance × area (RA) product, which is the resistivity times the film thickness, may also be large, resulting in excessive shot noise. Shot noise is intrinsic to tunneling with the direct-current (DC) bias current required for GMR head operation and is the dominant noise source in the TMR head. Figure 51.44 is a plot of the TMR ratio in % versus the RA product for three different TMR structures all made from the basic structure: buffer/PtMn/CoFe/Ru/CoFe/AlO_x/CoFe/NiFe/cap [51.93]. The PtMn is an antiferromagnet, CoFe/Ru/CoFe is a synthetic antiferromagnet, AlO_x is the insulating barrier (prepared by in situ oxidation) and CoFe/NiFe is the second electrode. The data points for TMR versus RA for this structure are labeled "Conv-btm" (conventional bottom) and the data points for the "Smooth-top" structure is for the PtMn layer on top

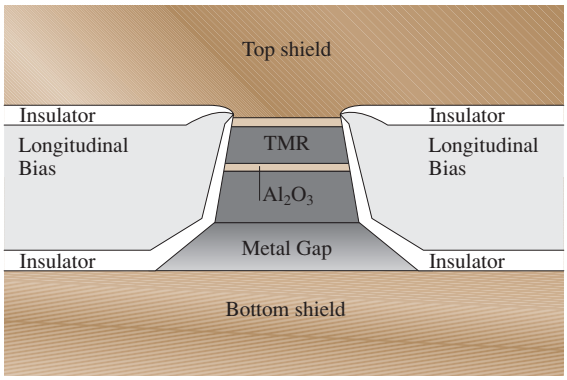

Fig. 51.43 Schematic drawing of the air-bearing surface view of a tunneling magnetoresistive (TMR) head. (After [51.93])

instead of the bottom, while the "Smooth-btm" data points are for a head made with smoother interfaces. The TMR % remains constant at ≈ 20% until a knee, below which the TMR % drops due to pinholes and incomplete insulation coverage. The stack of films is ion-milled and the stripe height is defined by lapping. Magnetic recording results showed the expected large signal ($V_{\text{peak-to-peak}} = 42\,\text{mV}/\mu\text{m}$) with a biasing current of 1 mA but the SNR was only 23.4 dB and was not deemed sufficient to demonstrate the required low error rate [51.93]. A significant problem with the TMR head is that there is a large resistance in parallel with the

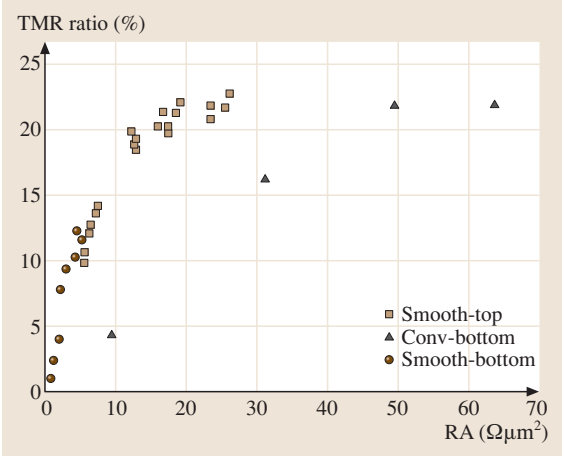

Fig. 51.44 Correlation between TMR ratio and resistance area product (RA) in three structures: top- and bottom-type MTJ with smoother interfaces and bottom-type MTJ with conventional stacking that has relatively rough interfaces. (After [51.93])

large capacitance resulting from the tunneling barrier. This combination results in a low-pass filter and care is required to limit the capacitance. In the example discussed here the cut off linear density is near 580 kfc/in. Because of the significantly larger value of ΔR for the CPP as opposed to the CIP technology, it is possible that CPP may become the dominant technology for read heads in the future.

51.3 Extraordinary Magnetoresistance (EMR)

An interesting development in read head technology is the discovery that narrow band gap and hence high-mobility semiconductors can be made to function as detectors of magnetic field [51.94]. The concept is based on the Lorentz force exerted on charge carriers by a megnetic field

$$F = q\bar{v} \times \bar{B} \,,$$

here q is the charge, $\bar{v}$ is the velocity of the charge carrier and $\bar{B}$ is the magnetic flux density acting on the charge. Electrons have the highest mobility as compared to holes and are the carriers used. The electrons are driven by an external source similar to the sense current in GMR sensors in a high mobility semiconductor and are deflected by the external magnetic field into a trajector and the voltage drop in the semiconductor at low locations is used to sense the magnetic field. The III–IV semiconductor InSb was chosen for the initial work on EMS because of the high mobility of electrons of 60 000 $cm^2/V\,s$. However, a major limitation was the ability to maintain the high mobility in thin films (< 100 nm) required for read head applications and this was addressed by forming a thin-film quantum well heterostructure [51.94]. An advantage of such sensors is the lack of any magnetic noise since there are no magnetic materials involved in the head structure. No experimental results of such structures in read head applications has been reported. a review of EMR as magnetic field nanosensors has been reported by *S. Solin* [51.95].

51.4 Summary

It was the purpose of this chapter to review the current status of the technology of magnetic recording as used in disk drives. The emphasis was on the magnetic materials used in the application and on some of the technical problems that may limit the increase in areal density of the devices. The new technology of MRAM, which has evolved from the magnetic recording application, was also reviewed. It was found that a wide range of magnetic materials is essential for the advance of magnetic recording and the MRAM technology, including high-magnetization soft-magnetic materials for write heads, new antiferromagnetic alloys with high blocking temperatures and low susceptibility to corrosion for pinning films in giant-magnetoresistive sensors and new ferromagnetic alloys with large values of giant magnetoresistance. A significant limitation to magnetic recording was found to be the superparamagnetic effect and new advances in multilayer ferromagnetic films to reduce the impact of the effect, but also to allow high-density recording, were discussed. Perpendicular recording as an alternative to longitudinal recording was reviewed and it was concluded that this technology will be the dominant recording technology in the future.

References

51.1 E. Grochowski: IBM Almaden Research Laboratories (http://www.storage.ibm.com/technolo/grochows/grocho01.htm) (2003)

51.2 R. L. Comstock: J. Mater. Sci. Mater. Electrom. **13**, 509 (2002)

51.3 C. D. Mee, E. D. Daniel, M. H. Clark: *Magnetic Recording: The First 100 Years* (Wiley, New York 1998)

51.4 R. L. Comstock: *Introduction to Magnetism and Magnetic Recording* (Wiley, New York 1999)

51.5 R. L. Comstock: *Data storage in rigid disks*, 2nd edn., ed. by C. Mee, E. Daniels (McGraw-Hill, New York 1996)

51.6 R. Bozorth: *Ferromagnetism* (Van Nostrand, New York 1951)(reprinted by IEEE, New York 1993)

51.7 X. Liu, G. Zangart, M. Shamsuzzoha: J. Electrochem. Soc. **150 (3)**, C159 (2003)
51.8 N. Robertson, B. Hu, C. Tsang: IEEE Trans. Magn. **33**, 2818 (1997)
51.9 X. Liu, G. Zangari: IEEE Trans. Magn. **37**, 1764 (2001)
51.10 T. Osaka, T. Yokoshima, T. Nakanishi: IEEE Trans. Magn. **37**, 1761 (2001)
51.11 Y. Liu, V. Harris, M. Kryder: IEEE Trans. Magn. **37**, 1779–1782 (2001)
51.12 Y. Ding, S. Byeon, C. Alexander Jr.: IEEE Trans. Magn. **37**, 1776 (2001)
51.13 R. E. Jones Jr.: IBM Disk Storage Technol. **GA-26-1665-0**, 6 (1980)
51.14 P. Andricacos, L. Romankiw: Magnetically soft materials in data storage: Their properties and electrochemistry. In: *Adv. Electrochem. Sci. Eng.*, Vol. 3, ed. by H. Gerischer, C. Tobias (VCH, Weinheim 1990)
51.15 R. L. Comstock, M. Williams: AIP Conf. Proc. Magn. Mater. **5**, 738 (1971)
51.16 T. Dinan: Electrolytics, Electrolytics Inc., San Jose Ca, private communication
51.17 G. Bertero, S. Malhotra, B. Bian, J. Tsoi, M. Avenell, D. Wachenschwanz, T. Yamashita: IEEE Trans. Magn. **39**, 651 (2003)
51.18 S. Byeon, F. Liu, G. Mankey: IEEE Trans. Magn. **37**, 1770 (2001)
51.19 M. Baibach, J. Broto, A. Fert, F. Nguyen Van Dan, F. Petroff, P. Etienne, G. Creuzet, A. Fredrick, J. Chazelas: Phys. Rev. Lett. **61**, 2472 (1988)
51.20 H. Kanai, K. Yamada, K. Aoshima, Y. Ohtsuka, J. Kane, M. Kanamine, J. Toda, Y. Mizoshita: IEEE Trans. Magn. **32**, 3368 (1996)
51.21 R. Wood, M. Williams, J. Hong: IEEE Trans. Magn. **26**, 2954 (1990)
51.22 B. Dieny, V. Speriosu, S. Parkin, P. Baumgart, D. Wilhoit: J. Appl. Phys. **69**, 4774 (1991)
51.23 S. Parkin: Appl. Phys. Lett. **61**, 1358 (1992)
51.24 H. Bertram, H. Zhou, R. Gustafson: IEEE Trans. Magn. **34**, 1846 (1998)
51.25 T. Lin, C. Tsang, R. Fontana, J. Howard: IEEE Trans. Magn. **32**, 2585 (1995)
51.26 A. Devasahayam, M. Kryder: IEEE Trans. Magn. **35**, 649 (1999)
51.27 Y. Hamakawa, M. Komuro, K. Watanabi, H. Hoshiya, T. Okada, K. Nakamoto, Y. Suzuki, M. Fuyama, H. Fukui: IEEE Trans. Magn. **35**, 677 (1999)
51.28 H. Kishi, Y. Kitade, Y. Miyaki, A. Tanaka, K. Kobayashi: IEEE Trans. Magn. **32**, 3380 (1996)
51.29 S. Parkin, D. Mauri: Phys. Rev. B **44**, 7131 (1991)
51.30 J. Mathon: Contemp. Phys. **32**, 143 (1999)
51.31 S. O. Kasap: *Principles of Electronic Materials and Devices*, 2nd edn. (McGraw-Hill, New York 2002)
51.32 I. A. Campbell, A. Fert: Transport properties of ferromagnets. In: *Ferromagnetic Materials*, Vol. 3, ed. by E. P. Wohlfarth (North-Holland, Amsterdam 1984) p. 3
51.33 R. C. O'Handley: *Modern Magnetic Materials Principles and Applications* (Wiley, New York 2000)
51.34 R. L. White: IEEE Trans. Magn. **28**, 2482 (1992)
51.35 M. Doerner, X. Bian, M. Madison, K. Tang, Q. Peng, A. Polcyn, T. Arnoldussen, M. Toney, M. Miramaani, K. Takano, E. Fullerton, D. Margulies, M. Schabes, K. Rubin, M. Pinarbasi, S. Yuan, M. Parker, D. Weller: IEEE Trans. Magn. **37**, 1052 (2001)
51.36 T. Arnoldussen: IEEE Trans. Magn. **34**, 1851 (1998)
51.37 G. Choe, J. Zhou, B. Demczyk, M. Yu, M. Zheng, R. Weng, A. Chekanov, K. Johnson, F. Liu, K. Stoev: IEEE Trans. Magn. **39**, 633 (2003)
51.38 M. Madison, T. Arnoldussen, M. Pinarbasi, T. Chang, M. Parker, J. Li, S. Duan, X. Bian, M. Mirzamaani, R. Payne, C. Fox, R. Wang: IEEE Trans. Magn. **35**, 695 (1999)
51.39 D. Weller, A. Moser: IEEE Trans. Magn. **35**, 4423 (1999)
51.40 E. Abarra, B. Acharya, A. Inomata, I. Okamoto: IEEE Trans. Magn. **37**, 1426 (2001)
51.41 E. Abarra, A. Inomata, H. Sato, I. Okamoto, Y. Mizoshita: Appl. Phys. Lett. **77**, 2581 (2000)
51.42 E. Fullerton, D. Margulies, N. Schabes, M. Carey, B. Gurney, A. Moser, M. Best, G. Zeltzer, K. Rubin, H. Rosen: Appl. Phys. Lett. **77**, 3806 (2000)
51.43 A. Inomata, B. Acharya, E. Abarra, A. Ajan, D. Hasegawa, I. Okamoto: J. Appl. Phys. **91**, 7671 (2002)
51.44 M. Schabes, E. Fullerton, D. Margulies: IEEE Trans. Magn. **37**, 1432 (2001)
51.45 IBM Research News (//www.research.ibm.com/esources/news/20010518_whitepaper.shtml) (2001)
51.46 Z. Zhang, Y. Feng, T. Clinton, G. Badran, N. Yeh, G. Tarnopolsky, E. Girt, M. Munteanu, S. Harkness, H. Richter, T. Nolan, R. Ranjan, S. Hwang, G. Rauch, M. Ghaly, D. Larson, E. Singleton, V. Vasko, J. Ho, F. Stageberg, V. Kong, K. Duxstad, S. Slade: IEEE Trans. Magn. **38**, 1861 (2002)
51.47 G. Choe, J. Zhou, R. Weng, K. Johnson: J. Appl. Phys. **91**, 7665 (2002)
51.48 S. Khizroev, Y. Lui, K. Mountfield, M. Kryder, D. Litvinov: J. Magn. Magn. Mater. **246**, 335 (2002)
51.49 M. Mallory, A. Torabi, M. Benaki: IEEE Trans. Magn. **38**, 1719 (2002)
51.50 M. L. Williams: Conf. Proc. IDEMA Symposium Perpendicular Recording, (2004)
51.51 W. Xia, H. Aoi, H. Muraoka, Y. Nakamura: IEEE Trans. Magn. **40**, 2365 (2004)
51.52 T. Okada, H. Kimura, I. Nunokawa, N. Yoshida, K. Etoh, M. Fuyama: IEEE Trans. Magn. **40**, 290 (2004)
51.53 N. Honda, K. Ouchi, S. Iwasaki: IEEE Trans. Magn. **38**, 1615 (2000)
51.54 K. Ouchi, N. Honda: IEEE Trans. Magn. **36**, 16 (2002)
51.55 N. Honda, S. Yanase, K. Ouchi, S. Iwasaki: J. Appl. Phys. **85**, 6130 (1999)

51.56 I. Lee, H. Ryu, H. Lee, T. Lee: J. Appl. Phys. **85**, 6133 (1999)
51.57 T. Kertoku, J. Ariake, N. Honda, K. Ouchi: J. Magn. Magn. Mater. **235**, 34 (2001)
51.58 L. Wu, S. Yanase, N. Honda, K. Ouchi: J. Magn. Soc. Jpn. **21**, 301 (1997)
51.59 X. Qi, B. Stadler, R. Victora, J. Judy, O. Hellwig, N. Supper: IEEE Trans. Magn. **40**, 2476 (2004)
51.60 T. Suzuki, N. Honda, K. Ouchi: J. Magn. Soc. Jpn. **21-S2**, 177 (1997)
51.61 G. Bertero, D. Wachenschwanz, S. Malhotia, S. Velu, B. Bian, D. Stafford, Y. Wu, T. Yamashita, S. Wang: IEEE Trans. Magn. **38**, 1627 (2002)
51.62 T. Oikawa, M. Nakamura, H. Uwazumi, T. Shimatsu, H. Muraoka, Y. Nakamura: IEEE Trans. Magn. **38**, 1976 (2002)
51.63 H. Uwazumi, K. Enomoto, Y. Sakai, S. Takenoiri, T. Oikawa, S. Watanabe: IEEE Trans. Magn. **39**, 1914 (2003)
51.64 Y. Sonobe, D. Weller, Y. Ikedu, K.. Takano, M. Schabes, G. Zeltzer, H. Do, R. Yeu, M. Best: J. Magn. Magn. Mater. **235**, 424 (2001)
51.65 Y. Sonobe, K. Miura, Y. Nakamura, K. Takano, H. Do, A. Mosher, B. Yen, Y. Ikeda, N. Supper: J. Appl. Phys. **91**, 8055 (2002)
51.66 H. Muraoku, Y. Sonobe, K. Muira, A. Goodman, Y. Nakamura: IEEE Trans. Magn. **38**, 1632 (2002)
51.67 Y. Sonobe, H. Muraoka, K. Miura, Y. Nakamura, K. Takano, A. Moser, H. Do, B. Yen, Y. Ikeda, N. Supper, H. Weresin: IEEE Trans. Magn. **38**, 2006 (2002)
51.68 M. Williams, C. Rettner, K. Takano, W. Weresin: IEEE Trans. Magn. **38**, 1643 (2002)
51.69 R. M. White: *Introduction to Magnetic Recording* (IEEE, New York 1985)
51.70 K. Z. Gao, H. N. Bertram: IEEE Trans. Magn. **38**, 3675 (2002)
51.71 J. Judy: J. Magn. Magn. Mater. **235**, 235 (2001)
51.72 E. Velua, S. Malhotra, G. Bertero, D. Wachenschwanz: IEEE Trans. Magn. **39**, 668 (2003)
51.73 S. Oikawa, A. Takeo, T. Hikosaka, Y. Tanaka: IEEE Trans. Magn. **36**, 2393 (2000)
51.74 M. Zheng, G. Choe, A. Chekanov, B. Demczyk, B. Acharya, K. Johnson: IEEE Trans. Magn. **39**, 1919 (2003)
51.75 K. Miura, H. Muraoka, Y. Sonobe, Y. Nakamura: IEEE Trans. Magn. **38**, 2054 (2002)
51.76 C. Brucker, T. Nolan, B. Lu, Y. Kubota, M. Plumer, P. Lu, R. Cronch, C. Chang, D. Chen, J. Chen, R. Michel, G. Parker, N. Tabat: IEEE Trans. Magn. **39**, 673 (2003)
51.77 C. Chang, M. Plumer, C. Brucker, J. Chen, R. Ranjan, J. van Elk, J. Yu, D. Karns, Y. Kubota, G. Ju, D. Weller: IEEE Trans. Magn. **38**, 1637 (2002)
51.78 M. Zheng, G. Choe, K. Johnson, L. Gao, S. Liou: IEEE Trans. Magn. **38**, 1979 (2002)
51.79 S. Kong, T. Okamoto, K. Kim, S. Nakagawa: IEEE Trans. Magn. **38**, 1982 (2002)
51.80 S. Takenoiri, K. Enomoto, Y. Sakai, S. Watanabe: IEEE Trans. Magn. **38**, 1991 (2002)
51.81 H. Takano, Y. Nishida, A. Kuroda, H. Sawaguchi, Y. Hosoe, T. Kawabe, H. Aoi, H. Muraoka, Y. Nakamura, K. Ouchi: J. Magn. Magn. Mater. **235**, 241 (2001)
51.82 W. Eppler, A. Sunder, D. Karns, E. Kurtas, G. Ju, X. Wu, P. van der Heijden, Y. Kubota, H. Zhou, C.-H. Chang: IEEE Trans. Magn. **39**, 663 (2003)
51.83 Hitachi Global Storage Technologies, announcement on the website; www.hitachigst.com/hdd/research/recording_head/pr (March 2005)
51.84 Seagate press release: seagate.com, (2002)
51.85 E. Murdock, J van Ek: Lake arrowhead workshop (2003)
51.86 S. Parkin, K. Roche, M. Samant, P. Rice, R. Beyers, R. Scheuerlein, E. O'Sullivan, S. Brown, J. Bucchigano, D. Abraham, Y. Lu, M. Rooks, P. Trouilloud, R. Wanner, W. Gallagher: J. Appl. Phys. **85**, 5828 (1999)
51.87 S. Tehrani, B. Engel, J. Slaughter, E. Chen, M. DeHerra, M. Durlam, P. Naji, R. Whig, J. Janesky, J. Calder: IEEE Trans. Magn. **36**, 2752 (2000). The curve of magnetoresistance % is from a private communication with Mark deHerrera from Motorola
51.88 R. Meservey, P. Tedrow: Phys. Rep. **238**, 175 (1994)
51.89 M. Julliere: Phys. Lett. **54A**, 225 (1975)
51.90 H. Kronmüller, R. Hertel: J. Magn. Magn. Mater. **215-216**, 11 (2000)
51.91 K. Lee, W. Park, T. Kim: IEEE Trans. Magn. **39**, 2842 (2003)
51.92 I. Prejbeanu, W. Kula, K. Ounadjela, R. Sousa, O. Redon, B. Dieny, J. Nozieres: IEEE Trans. Magn. **40**, 2625 (2004)
51.93 S. Araki, K. Sato, T. Kagami, S. Saruki, T. Uesugi, N. Kasahara, T. Kuwashima, N. Ohta, J. Sun, K. Nagi, S. Li, N. Hachisuka, H. Hatata, N. Kagotani, N. Takahashi, K. Ueda, M. Matsuzaki: IEEE Trans. Magn. **38**, 72 (2002)
51.94 S. Solin, D. Hines, A. Rowe, J. Tsai, Y. Pashkin, S. Chung, N. Goel, M. Santos: Appl. Phys. Lett. **80**, 4012 (2002)
51.95 S. Solin: Sci. Am. Mag. **291**, 71 (2004)